Agricultural and Forest Meteorology 295 (2020) 108169

Contents lists available at ScienceDirect

Agricultural and Forest Meteorology

journal homepage: www.elsevier.com/locate/agrformet

Simulating spatially distributed solar-induced chlorophyll fluorescence using a BEPS-SCOPE coupling framework

Tianxiang Cui[a,b,c], Rui Sun[b,c,*], Zhiqiang Xiao[b,c], Ziyu Liang[a], Jian Wang[d]

[a] College of Forestry, Nanjing Forestry University, Nanjing, Jiangsu 210042, China
[b] State Key Laboratory of Remote Sensing Science, Faculty of Geographical Science, Beijing Normal University, Beijing 100875, China
[c] Beijing Engineering Research Center for Global Land Remote Sensing Products, Faculty of Geographical Science, Beijing Normal University, Beijing 100875, China
[d] College of Information and Management Science, Henan Agricultural University, Zhengzhou, Henan 450002, China

ARTICLE INFO

Keywords:
Solar-induced chlorophyll fluorescence (SIF)
Photosynthesis
BEPS
SCOPE
Coupling model
Spatial simulation

ABSTRACT

Remotely sensed solar-induced chlorophyll fluorescence (SIF) has been increasingly used to probe photosynthesis and model the gross primary productivity (GPP). Although SIF at the top of canopy (TOC) can be simulated using the coupled photosynthesis-fluorescence model SCOPE (Soil Canopy Observation, Photochemistry and Energy fluxes), simulating spatially distributed TOC SIF usually requires extensive calculations, entailing some challenges when applying the model to the regional and the global scales. This study puts forward a coupling framework that combines SIF and global terrestrial biosphere models (TBMs). The theory for fluorescence emissions and the fluorescence radiative transfer algorithm described in the SCOPE model were integrated with the "two-leaf"-based BEPS (Boreal Ecosystem Productivity Simulator) model. To simplify the fluorescence radiative transfer physics, we put forward a canopy-averaged leaf-level fluorescence to represent the fluorescence emitted from sunlit and shaded leaf groups and performed a sensitivity analysis to assess the determining factors in upscaling fluorescence from leaf scale to canopy scale. We found that the relationship between the leaf and canopy fluorescence at 740 nm was mainly affected by LAI. Although brown pigments and leaf inclination angle demonstrate some impacts on the scaling process, an LAI-based coefficient can well characterize the upscaling from leaf to canopy scale. Since our BEPS-SCOPE coupling model deploys the sunlit-shaded leaf separation strategy, we expect that it can efficiently characterize the nonlinear responses of photosynthesis and the associated fluorescence to environmental factors. The performance of our model was evaluated at both site and global scales, which demonstrated a good performance for most plant functional types (PFTs) except for needleleaf types that have a more clumped nature. Apart from these limitations, the presented model can contribute to efficiently simulating SIF at regional and global scales, and has the potential to reduce uncertainties in GPP estimation.

1. Introduction

Plant photosynthesis is an important process that assimilates CO_2 and mediates most of the carbon and water fluxes in the biosphere-atmosphere system. Spatially simulating photosynthesis at the ecosystem scale (Gross Primary Productivity, GPP) can therefore provide essential insights for understanding terrestrial ecosystem functions, carbon and water cycling, and climate change (Thurner et al., 2014). In the past decades, solar-induced chlorophyll fluorescence (SIF) has been increasingly used to probe photosynthesis and estimate GPP as it is directly linked to the photosynthetic process. It is sensitive in tracking the regulatory processes in photosynthesis under variable environmental conditions such as light, water, heat and nutrition stresses, making it more effective in tracking the actual photosynthetic rates than the reflectance-based data as reflectance-based data are generally used to estimate plant potential photosynthetic rates (Guanter et al., 2014; Damm et al., 2015; Porcar-Castell et al., 2014).

SIF is energy emitted as one dissipative pathway that competes with photochemistry and heat dissipation (non-photochemical quenching, NPQ) after chlorophyll molecules absorb the photosynthetically active radiation (PAR) (Baker, 2008). Due to the competitive relationship among SIF, photosynthesis, and NPQ, the recent development of passively measuring SIF has created a novel method for spatially monitoring GPP (Porcar-Castell et al., 2014; Zarco-Tejada et al., 2013). Currently, globally SIF can be generated using satellite-based sensors such as GOSAT TANSO-FTS, ENVISAT SCIAMACHY, MetOp-A/B

* Corresponding author at: State Key Laboratory of Remote Sensing Science, Faculty of Geographical Science, Beijing Normal University, Beijing 100875, China.
E-mail address: sunrui@bnu.edu.cn (R. Sun).

https://doi.org/10.1016/j.agrformet.2020.108169
Received 17 November 2019; Received in revised form 26 August 2020; Accepted 27 August 2020
Available online 09 September 2020
0168-1923/ © 2020 The Author(s). Published by Elsevier B.V. This is an open access article under the CC BY-NC-ND license (http://creativecommons.org/licenses/by-nc-nd/4.0/).

GOME-2, OCO-2, TanSat ACGS, and Sentinel-5P TROPOMI (Joiner et al., 2011, 2013, 2016; Frankenberg et al., 2011, 2014; Du et al., 2018; Liu et al., 2018b; Guanter et al., 2015; Köhler et al., 2018). Although none of these sensors were initially planned for SIF monitoring, strong linear relationships between satellite-based SIF and remotely-sensed GPP products or GPP derived from EC (Eddy Covariance) towers have been discovered (Frankenberg et al., 2011; Guanter et al., 2014; Sun et al., 2017, 2018; Yang et al., 2015). Additionally, former studies have also shown that SIF performs well in capturing plant phenology (Jeong et al., 2017; Joiner et al., 2014). Recent literature has even suggested that the SIF-GPP relationship is consistent under different vegetation types (Sun et al., 2017; Li et al., 2018b). Despite these promising insights, the underlying mechanism of these correlations has not yet been well-established (Porcar-Castell et al., 2014; Mohammed et al., 2019). For instance, it is well accepted in recent literature that the SIF-GPP relationship is influenced by observational wavelength (Verrelst et al., 2016), temporal scaling (Zhang et al., 2016b, 2018a), chlorophyll content (Liu et al., 2016a; Liu et al., 2017b), canopy structure (Damm et al., 2015), light condition (Damm et al., 2015; van der Tol et al., 2014; He et al., 2017), stress status (van der Tol et al., 2014), and orbital geometry (Joiner et al., 2020). We expect that these various factors can lead to complex SIF-GPP relationships. Thus, to properly utilize remotely sensed SIF observations in tracking terrestrial GPP, physiological theories need to be considered together with SIF observations.

SIF can be simulated with the Soil Canopy Observation, Photochemistry and Energy fluxes (SCOPE) model (van der Tol et al., 2009). SCOPE deploys the typical FvCB biochemical model (Farquhar et al., 1980) when modeling photosynthesis for C3 and C4 species. The fluorescence emission theory used in the model is based on the work of Lee et al. (2013, 2015) and van der Tol et al. (2014), in which the relationship between leaf photosynthesis and chlorophyll fluorescence was described using an empirical approach. SCOPE also adopts the FluorSAIL theory (van der Tol et al., 2019) to describe the fluorescence radiative transfer process. A complete run of SCOPE estimates the carbon, water and energy fluxes, as well as canopy optical, thermal, and fluorescence spectra. Due to its high computational demand, SCOPE is not suitable for regional and global SIF simulations. In recent years, SIF has been integrated with global terrestrial biosphere models (TBMs), such as CLM4 (Community Land Model Version 4), SSiB2 (Simplified Simple Biosphere Model version 2), BEPS (Boreal Ecosystem Productivity Simulator), ORCHIDEE (Organizing Carbon and Hydrology In Dynamic Ecosystems), BETHY (Biosphere Energy Transfer Hydrology), and JSBACH (Jena Scheme for Biosphere-Atmosphere Coupling in Hamburg) (Lee et al., 2015; Raczka et al., 2019; Qiu et al., 2018, 2019; Bacour et al., 2019; Norton et al., 2019; Thum et al., 2017). These studies enable spatially explicit, plant functional type (PFT) dependent global simulations of GPP and SIF, which also laid the basis for evaluating and improving our understanding of global carbon cycle (Koffi et al., 2015; Norton et al., 2019). The general ideas of these SIF-TBMs are: (1) to integrate a model that describes the relationship between fluorescence and photosynthesis at leaf scale, (2) to deploy a canopy radiative transfer model to upscale fluorescence from leaf scale to canopy scale (Parazoo et al., 2020). Thus, accurately estimating photosynthesis and the coupled energy exchange, evapotranspiration is the prerequisite and basis for the SIF-TBMs. Additionally, simplifying the fluorescence radiative transfer process is necessary for improving the computational efficiency in regional and global simulations.

In general, TBMs can be categorized as big-leaf, two-leaf, and multilayer models. Compared with the two-leaf model that treats vegetation canopy as two groups of leaves, sunlit and shaded ones, the big-leaf approach has been proven to lead to underestimated results in modeling canopy GPP as it excludes the photosynthetic contributions of shaded leaf groups (Chen et al., 1999). Additionally, some studies have noted that SIF is more related to sunlit-leaf GPP than total or shaded GPP because the fluorescence yield and photosynthetic efficiency are positively related at stressed or high-light conditions, while under low-light unstressed situations, their relationship becomes competitive (Damm et al., 2015; Wang 2014). These existing studies suggest the necessity of separating canopy leaves into sunlit and shaded groups when using SIF to model the canopy photosynthesis process or vice versa. Although the multilayer model is more adequate in simulating GPP (De Pury and Farquhar, 1997; Reick et al., 2013), the two-leaf model has been proven to be more computationally effective when compared with the multilayer theory (Wang and Leuning, 1998) and can adequately capture the variations in the leaf biochemical characteristics within the entire canopy (Chen et al., 2012; Zhang et al., 2012; Wang and Leuning, 1998). In fact, apart from ORCHIDEE deploys the big-leaf model, BETHY and JSBACH adopt the multilayer model, most of the existing SIF-TBMs (CLM4, SSiB2, BEPS) employ the two-leaf approach in modelling canopy SIF and GPP.

The fluorescence model described in the SIF-TBMs typically adopts the theories of Lee et al. (2013, 2015) and van der Tol et al. (2014) in which the relationship between fluorescence and photosynthesis at leaf scale is described as a function of environment conditions. Although SIF emission is directly linked with photosynthesis at leaf scale, the TOC SIF is affected by the leaf optical properties and the canopy structural variables (Verrelst et al., 2015). Therefore, studies of scaling processes between leaf and canopy fluorescence are essential in characterizing the relationship between GPP and remotely sensed wavelength-dependent TOC SIF (Liu et al., 2020). Recently, Yang and van der Tol (2018) noted that the canopy scattering of red TOC SIF is more affected by leaf pigments while the far-red TOC SIF is more sensitive to canopy LAI. A further study conducted by van der Tol et al. (2019) suggested that leaf brown material and dry matter affect the escape probability of fluorescence from canopy at far-red region. To characterize the scaling process between leaf and canopy fluorescence, Zeng et al. (2019) deployed the near-infrared reflectance of vegetation (NIRv) and FPAR (fraction of absorbed photosynthetically active radiation) to estimate the escape ratio of far-red SIF. Qiu et al. (2019) put forward a fluorescence upscaling approach that considered canopy extinction and scattering. These studies have simplified the fluorescence radiative transfer process and shown enormous potentials in efficiently upscaling fluorescence from leaf to canopy scale. Apart from these studies, other studies have put forward an upscaling factor to describes the relationship between leaf and canopy fluorescence (Lee et al., 2015; Thum et al., 2017; Raczka et al., 2019; Qiu et al., 2019; Parazoo et al., 2020). In the reported literature, the upscaling factor is commonly related to the maximum carboxylation capacity (V_{cmax}) (Lee et al., 2015; Raczka et al., 2019), LAI (Qiu et al., 2019; Thum et al., 2017) or solar zenith angle (SZA) (Qiu et al., 2019). As the upscaling factor occupies various forms, it is still necessary to assess the factors that mostly affect the fluorescence upscaling process from leaf to canopy in the SIF-TBMs, especially for a two-leaf based model that is more efficient in regional and global simulations.

In this study, we propose an approach for coupling fluorescence to photosynthesis in the two-leaf based BEPS model. The coupling model incorporates the theories of both BEPS and SCOPE. The fluorescence model proposed by Lee et al. (2013, 2015) and van der Tol et al. (2014) is integrated, and simplified upscaling factor is then introduced after performing a series of sensitivity analyses. Our model was evaluated at both the site and global scales. The presented model serves to efficiently simulate SIF at regional and global scales, and can be applied to assess the performance of BEPS in modeling GPP and the coupling processes by comparing the simulated SIF with the observed SIF. In recent studies, Koffi et al. (2015) and Norton et al. (2019) discussed the possibility of combining the observed SIF with process-based models to improve the estimation of GPP using data assimilation techniques. In this context, the presented model can also serve to potentially reduce uncertainties in GPP by optimizing model parameters.

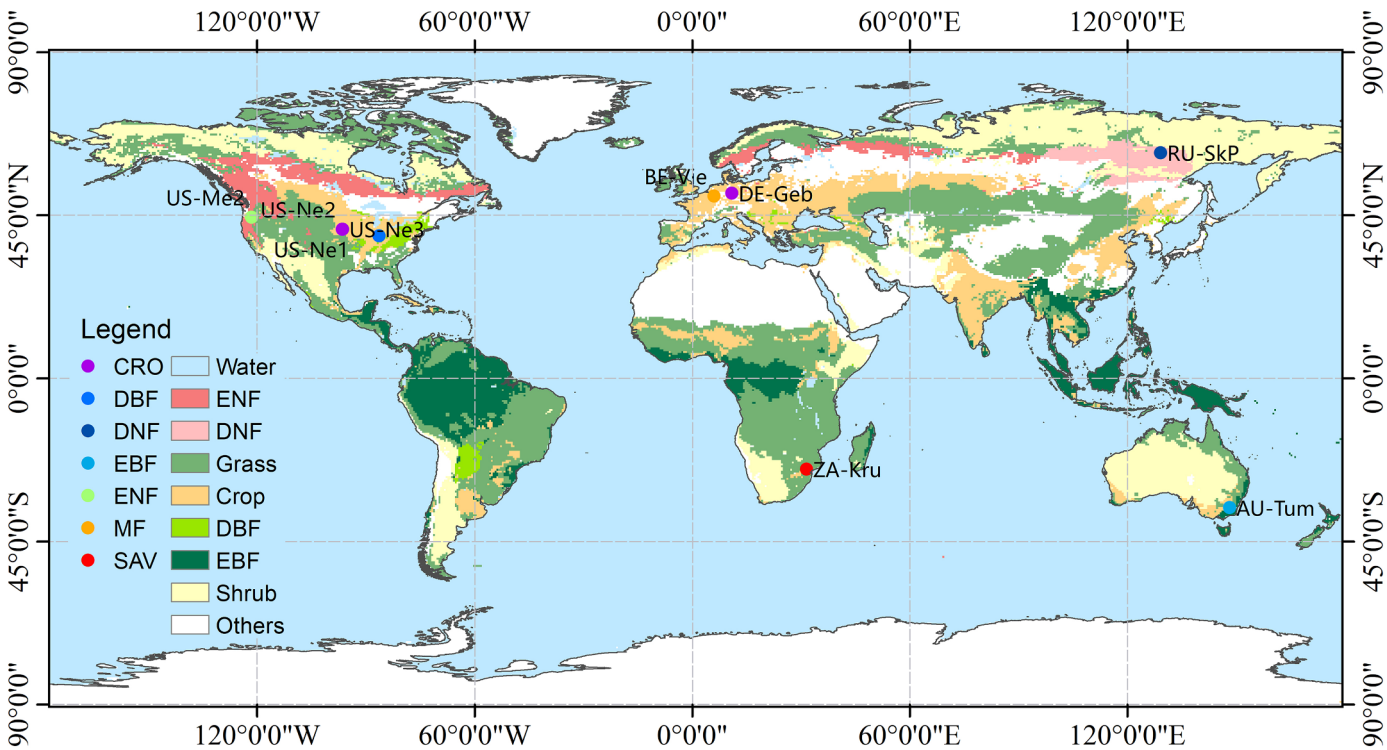

Fig. 1. Spatial distribution of the selected sites.

2. Materials

2.1. Datasets for site-scale simulation

2.1.1. Meteorological data

We used ten flux tower sites belonging to the FLUXNET 2015 dataset in this study. FLUXNET provides site-scale measurements of carbon, water and energy fluxes using the eddy covariance (EC) technique (Baldocchi et al., 2001), as well as measurements of the meteorological data. The FLUXNET 2015 dataset contains 212 sites distributed around the world with most of the world's climate types and representative biomes. The EC fluxes data are provided with five temporal aggregations of half-hourly or hourly, daily, weekly, monthly and yearly (Pastorello et al., 2017). For our study, seven types of biomes located around the world containing evergreen broadleaf forest (EBF), evergreen needleleaf forest (ENF), deciduous broadleaf forest (DBF), deciduous needleleaf forest (DNF), mixed forest (MF), cropland (CRO) and savanna (SAV) were included in the ten selected EC flux tower sites (Fig. 1). To ensure land surface uniformity around each site, the MODIS product for land-cover types (MCD12Q1) (Friedl et al., 2010) was used to investigate the spatial homogeneity within the GOME-2 footprint. For each selected site in our study, the dominant vegetation-cover type at the flux site exceed 60% of the GOME-2 grid cell (Table 1). To perform our simulation, the measured hourly meteorological factors including incoming shortwave radiation, air temperature, precipitation, and wind speed were extracted.

2.1.2. Leaf area index (LAI) data

For our site-scale simulation, we employed the Global LAnd Surface Satellite (GLASS) product for LAI to derive LAI for each site. GLASS LAI is generated based on the General Regression Neural Networks (GRNNs) with land surface reflectance data obtained by MODIS and Advanced Very High Resolution Radiometer (AVHRR) (Xiao et al., 2014, 2016). In former evaluations, the GLASS LAI was temporally smoother and perceived as having a higher quality and accuracy than both the MODIS LAI product (MOD15) and the Geoland2/BioPar version 1 (GEOV1) LAI product (Xiao et al., 2016). By considering data availability, the retrieval of the 8-day GLASS LAI deploys the AVHRR and the MODIS reflectance data to generate LAI at spatial resolutions of 0.05° and 1 km, respectively. The 0.05° version spans from 1982 to 2017, and the 1 km version covers 2000 to 2017. In our study, LAI values at the site-scale were obtained using the 1 km version.

As the GLASS LAI might be contaminated by clouds, a temporal gap-filling algorithm was performed for the original time-series LAI. First,

Table 1
Details of the selected EC sites in this study.

Site ID	Lat.	Lon.	IGBP class	Study period	max(LC) (%)	Reference
AU-Tum	-35.657	148.152	EBF	2007~2013	0.6092	Leuning et al. (2005)
BE-Vie	50.305	5.998	MF	2007~2014	0.9448	Aubinet et al. (2001)
DE-Geb	51.100	10.914	CRO	2007~2014	0.8380	Anthoni et al. (2004)
RU-SkP	62.255	129.168	DNF	2012~2014	0.6181	-
US-Me2	44.452	-121.557	ENF	2007~2014	0.6914	Campbell and Law (2005)
US-MMS	39.323	-86.413	DBF	2007~2014	0.5066	Sims et al. (2005)
US-Ne1	41.165	-96.477	CRO	2007~2012	0.9584	Suyker et al. (2005)
US-Ne2	41.165	-96.470	CRO	2007~2012	0.9574	Suyker et al. (2005)
US-Ne3	41.180	-96.440	CRO	2007~2012	0.9377	Suyker et al. (2005)
ZA-Kru	-25.020	31.494	SAV	2009~2013	0.9490	Archibald et al. (2009)

we performed a data quality check with the quality flag layer of the product, and observations not influenced by clouds were treated as high quality (cloud state is clear). A linear interpolation algorithm was then applied to generate temporally continuous daily LAI values using only high-quality data. Finally, a Savitzky-Golay filter was used to smooth the data and eliminate high-frequency noise (Zhang et al., 2016a).

2.2. Datasets for the global simulation

2.2.1. Global leaf area index (LAI) data

The GLASS LAI dataset from 2012 at a 0.05° spatial resolution was selected to perform our global simulation. The formerly mentioned temporal gap-filling algorithm was also performed on the original data to generate the daily globally distributed LAI. Notably, some pixels had less than 3 out of 46 good retrievals for one year globally. As these pixels only occupied a small percentage of the total pixels (< 0.5%), we kept their original values in the research. The gap-filled LAI was then aggregated to a 0.5° spatial resolution as inputs to our model.

2.2.2. Global land-cover data

We used the MODIS land-cover type climate modeling grid product (MCD12C1) version 6 in the study (Sulla-Menashe and Friedl, 2018). Each MCD12C1 pixel represents the annually dominant land-cover type within a 0.05° × 0.05° grid cell. The MCD12C1 was derived based on a decision-tree classification algorithm using MODIS data acquired with both Terra and Aqua (Friedl et al., 2010). In our study, the 2013 MCD12C1 data was used to represent the land-cover situation in 2012. The IGBP land-cover classification scheme in the dataset was obtained to provide biome-specific information for our coupling model.

To perform our simulation at a 0.5° resolution, the 0.05° MCD12C1-based IGBP land-cover type data were spatially aggregated to a 0.5° resolution based on the maximum area rule. Specifically, the frequency of individual land-cover type within a 0.5° × 0.5° area was calculated, and the dominant type was assigned as the cell value.

2.2.3. Global meteorological data

Globally distributed meteorological data were obtained from Global Land Data Assimilation System (GLDAS) products (Rodell et al., 2004). By deploying land surface process models and data assimilation algorithms, GLDAS provides meteorological information of land surface for the entire globe with both 3-hourly and monthly temporal resolutions. The spatial resolutions of this meteorological dataset contain both the 0.25° and 1.0° versions. For our global simulation, we used the 3-hourly 0.25° dataset (GLDAS-2.1 Noah 0.25° 3-hourly), which was generated using the Noah model 3.3 in Land Information System (LIS) Version 7 (Rodell et al., 2004). The incoming shortwave radiation, air temperature, specific humility, precipitation and wind speed were extracted. These GLDAS-based meteorological data were all spatially aggregated to a 0.5° resolution to match our simulation.

We also obtained the GLDAS-based soil temperature, soil moisture and snow depth to drive our model. For soil temperature and soil moisture, the GLDAS product provides four vertical levels, including 1–10, 10–40, 40–100, and 100–200 cm. Notably, the soil moisture data defined in the GLDAS product were the average layer soil moisture (kg/m^2) rather than the volumetric soil moisture (m^3/m^3). To match the model inputs, we selected the soil temperature and soil moisture at the top layer (0-10 cm) for our research. The GLDAS-based top layer soil moisture (kg/m^2) was used to convert to a volumetric soil moisture (m^3/m^3).

2.2.4. Global soil texture data

For global simulation, we used the soil texture data of the Harmonized World Soil Database (HWSD) v1.2. This dataset was provided at spatial resolution of 30 arc-second (or ~1 km) (Nachtergaele et al., 2010). We regridded the HWSD soil texture data from their native grid resolution to 0.5° by assigning the dominant soil texture type to the grid cell within a 0.5° × 0.5° area.

2.3. Datasets used to evaluate and compare simulations

2.3.1. EC data from FLUXNET tower sites

The EC data of the selected FLUXNET tower sites were used to evaluate our site-scale simulation. As the FLUXNET 2015 dataset provided two types of GPP estimations, the daytime method (Lasslop et al., 2010) and the nighttime method (Reichstein et al. 2003), we first performed a simple comparison between these two methods. For our selected sites, the monthly averaged daily GPP based on the nighttime partitioning was strongly correlated with that based on the daytime partitioning (R^2 = 0.968, Fig. S1). Thus, we considered both methods to have small differences in GPP estimation and used the monthly GPP generated with the nighttime partitioning methods in our research.

2.3.2. GOME-2 SIF product

The SIF product retrieved with the Global Ozone Monitoring Experiment 2 (GOME-2) spectrometer onboard the EUMETSAT's MetOp-A was deployed for a comparison with the simulated SIF in our study (Joiner et al., 2013, 2016). The MetOp-A runs in a polar sun-synchronous orbit, crossing the equator southbound at approximately 9:30 am. The nadir footprint of GOME-2 onboard MetOp-A was initially 80 km × 40 km, and was reduced to 40 km × 40 km after July 2013. GOME-2 measures the radiance at the top-of-atmosphere between 240 and 790 nm with a spectral resolution of 0.2-0.4 nm. The Channel 4 covers wavelengths between 734 and 758 nm with an approximately 0.5 nm spectral resolution was used to retrieve far-red SIF at approximately 740 nm (Joiner et al., 2011, 2013, 2016). Compared with the GOME-2 daily product (Level 2) that is generally contaminated by an inherent noise due to low SNR (Joiner et al., 2013, 2016), the 0.5° Level 3 monthly SIF product (v27) has been quality-filtered and monthly averaged, which increases the SNR and enables effective model evaluation. We used the instantaneous monthly SIF data from 2007 to 2015 in the study. The daily averaged SIF in 2012 that corrected the variability of photosynthetically active radiation (PAR) in the Level 3 monthly product was also extracted.

2.3.3. SCOPE simulated SIF

As the SCOPE model is too computationally expensive for global applications, we only performed site-scale simulation with SCOPE to assess our model. Apart from the meteorological data provided by FLUXNET and the GLASS LAI, we also adopted PFT-specific V_{cmax} (maximum carboxylation capacity) and C_{ab} (chlorophyll content) in the site-scale SCOPE simulations by referring to Chen et al. (2012), Zhang et al. (2014), and Koffi et al. (2015). The main input parameters for the simulations are listed in Table S1.

3. Methodology

3.1. BEPS model

The BEPS model is a process-based model that deploys the two-leaf upscaling strategy in generating the canopy-level GPP. It adopts the FvCB photosynthesis model (Farquhar et al., 1980) in estimating leaf-level photosynthesis, and calculates the canopy-level GPP by adding the photosynthesis rates of sunlit and shaded leaves. This model has been deployed to estimate GPP/NPP for different PFTs across regional and global and demonstrated reasonable performance (Chen et al., 2012; Feng et al., 2007; Matsushita and Tamura, 2002; Zhang et al., 2012). The BEPS model can be run at both daily and hourly scale. In comparison with the daily version which treats leaf temperature as air temperature, the hourly version, by contrast, generates leaf temperature using an iterative algorithm that deploys the canopy energy balance theory (Ju et al., 2006). Despite its intense computational requirements, we used the hourly version of BEPS in the study to generate

SIF signal at the MetOp-A satellite overpass time (~ 9:30 am) as SIF demonstrates significant diurnal variation characteristics (Cui et al., 2017; Liu et al., 2017a; Zhang et al., 2018a).

By adopting the two-leaf theory, the BEPS model is more effective in generating canopy photosynthesis than the conventional big-leaf model because it can more adequately capture the nonlinear responses of water, heat, and CO_2 fluxes to environmental factors (Chen et al., 1999). Canopy photosynthetic rate can be modeled using:

$$A_{\text{canopy}} = A_{\text{su}} LAI_{\text{su}} + A_{\text{sh}} LAI_{\text{sh}} \tag{1}$$

where the subscripts su and sh indicate the sunlit and shaded leaf groups, respectively.

The photosynthetic rates for these two leaf groups are calculated with the FvCB photosynthesis model (Farquhar et al., 1980) and the theory of Collatz et al. (1992) for C3 and C4 species, respectively:

$$w_c = \begin{cases} V_m \frac{C_i - \Gamma}{C_i + K} & \text{forC3} \\ V_m & \text{forC4} \end{cases} \tag{2}$$

$$w_e = \begin{cases} J \frac{C_i - \Gamma}{4.5C_i + 10.5\Gamma} & \text{forC3} \\ J & \text{forC4} \end{cases} \tag{3}$$

$$w_s = \begin{cases} V_m/2 & \text{forC3} \\ 2 \times 10^4 V_m C_i/P & \text{forC4} \end{cases} \tag{4}$$

$$A = \min(w_c, w_e, w_s) - R_d \tag{5}$$

where the terms w_c, w_e and w_s represent the photosynthetic rates under different limited cases (w_c, carboxylation rate limited case; w_e, electron transport or RuBP regeneration limited case; w_s, phosphate limited or export of the photosynthetic products limited case). The net photosynthetic assimilation rate, A, is treated as the minimum of these three rates minus the dark respiration rate, R_d. The terms w_c, w_e and w_s are expressed as functions of the kinetic constraints, irradiation conditions, and CO_2 partial pressure with C_i, Γ, K, V_m, J and P representing the CO_2 concentration in the intercellular airspace, the CO_2 compensation point, the Michaelis-Menten coefficient, the maximum Rubisco activity rate, the electron transport rate and the atmospheric pressure, respectively.

In practice, the photosynthetic model is used in combination with the physical stomatal conductance model that describes the rate of CO_2 passing through leaf stomata. The stomatal conductance, g, in the BEPS model is described with a modified Ball-Berry equation that considers the influence of soil water (Ju et al., 2006):

$$g = f_w \left(m \frac{Ah_s}{C_s} p + b \right) \tag{6}$$

where m is a biome-specific coefficient, h_s, p, and C_s are the leaf surface relative humidity, the atmospheric pressure, and the leaf surface CO_2 concentration, respectively. b represents the minimum stomatal conductance when leaf photosynthesis is zero and can thus be generated by leaf dark respiration. The term f_w describes the impact of soil moisture on stomatal conductance by using the root-water uptake model proposed by Ju et al. (2006).

In the BEPS model, the LAI for sunlit and shaded leaf groups are calculated by extending Norman's method (1982) by considering the effect of foliage clumping. The incident radiations reaching these two types of leaf groups are generated by reducing the radiative transfer physics into simple equations. More details are provided in Chen et al. (1999, 2012).

3.2. SCOPE model

The SCOPE model links the radiative transfer, micrometeorological and biochemical processes to generate both canopy spectra (reflectance and SIF spectra) and energy balance fluxes (heat, water, and CO_2 fluxes) (van der Tol et al., 2009). We used the latest version (v1.70) to conduct our research. SCOPE deploys an extended PROSPECT model, Fluspect (Verhoef, 2011; Vilfan et al., 2016), in order to simulate the spectra of leaf reflectance, transmittance and fluorescence. The incident radiations that fall on leaves are generated by considering their position and orientation using the SAIL theory (Verhoef and Bach, 2007). Then, the incident radiation that reaches each canopy element is used to calculate the thermal radiation, energy balance fluxes and chlorophyll fluorescence. After obtaining the leaf-level thermal radiation and fluorescence, the TOC spectra of thermal and fluorescence radiations are derived based on the theory of Verhoef et al. (2007) and the FluoSAIL model (van der Tol et al., 2019), respectively.

Consistent with the BEPS model, SCOPE deploys the FvCB model and the theory of Collatz et al. (1992) in generating photosynthesis, which improves but does not guarantee consistency in predicted carbon, water, and energy fluxes between the two models (Dutta et al., 2019; Parazoo et al., 2020).

3.3. Model integration

3.3.1. Incorporation of photosynthesis and fluorescence

The SCOPE model uses the fluorescence emission efficiency (ε) to characterize the relationship between photosynthesis and fluorescence (Lee et al., 2013, 2015; van der Tol et al., 2014). Fluorescence emissions efficiency indicates the probability of fluorescence emission after absorbing PAR (Verrelst et al., 2015; Zhang et al., 2016b). In the SCOPE model, fluorescence generated by photosystem I (PS-I) is proportional to the absorbed photosynthetically active radiation (APAR), and ε is assumed to be constant. In contrast, the emissions efficiency of PS-II is treated as variable and is calculated using the semiempirical model proposed by Lee et al. (2013, 2015) and van der Tol et al. (2014). In their study, steady state fluorescence yield (Φ_F), electron transport rate and photosynthesis rate were linked by using numerical analysis based on the leaf-level gas exchange measurements and the corresponding active fluorescence data under various environmental situations. Since ε is directly proportional to Φ_F, the model allows us to generate the fluorescence emissions efficiency (ε) using the photochemical yield (Φ_P) at the leaf-level (Lee et al., 2013, 2015; van der Tol et al., 2014):

$$\varepsilon \propto \Phi_F = \Phi_{Fm}(1 - \Phi_P) \tag{7}$$

where Φ_{Fm} represents the fluorescence yield at saturating irradiance for a light-adapted leaf. This can be generated using:

$$\Phi_{Fm} = \frac{k_F}{k_F + k_D + k_N} \tag{8}$$

where k represents the quenching rate coefficient. Specifically, k_F indicates the rate coefficient for fluorescence, where k_D and k_N both represent heat dissipation with the former representing the constitutive one and the latter indicating the energy-dependent one that is determined by the electron transport rate.

By referring to van der Tol et al. (2014), k_F can be treated as a constant, k_D is modeled using a linear regression of temperature when temperature exceeds 26°C, and k_N is quantified using an empirical nonlinear relationship with a factor, x, that represents the light saturation degree of photosynthesis:

$$k_F = 0.05 \tag{9}$$

$$k_D = \max(0.03T + 0.0773, 0.87) \tag{10}$$

$$k_N = k_N^0 \frac{(1 + \beta)x^\alpha}{\beta + x^\alpha} \tag{11}$$

where k_N^0, α, and β are coefficients derived with experimental data. Two empirical calibrations for k_N are available according to van der Tol et al. (2014). For our study, we used the group of parameters calibrated with Flexas et al.'s (2002) experiment that was conducted on several plant species under different drought conditions with values 5.01, 1.93, and 10 for k_N^0, α, and β, respectively. The variable x is defined as:

$$x = 1 - \frac{\Phi_P}{\Phi_{P0}} \tag{12}$$

with Φ_P and Φ_{P0} indicating the actual and potential photochemistry yields, respectively. Φ_P can be generated using:

$$\Phi_P = \Phi_{P0}\frac{J_a}{J_e} \tag{13}$$

where J_a is the actual electron transport rate that can be calculated using the rate of gross CO_2 assimilation A (Eq. (5)), and J_e is the potential electron transport rate that is generated with APAR:

$$J_a = \begin{cases} \frac{1}{Eff_{C3}} A \frac{C_i + 2\Gamma}{C_i - \Gamma} & \text{forC3} \\ \frac{1}{Eff_{C4}} A & \text{forC4} \end{cases} \tag{14}$$

$$J_e = 0.5 \cdot \text{APAR} \cdot \Phi_{P0} \tag{15}$$

$$\Phi_{P0} = \frac{k_P}{k_P + k_F + k_D} \tag{16}$$

where $Eff_{C3} = 0.25$, $Eff_{C4} = 0.17$, and $k_P = 4.0$ (van der Tol et al., 2014).

Eq. (14) makes it possible to obtain J_a using the actual photosynthesis rate A. Consequently, the steady state fluorescence yield Φ_F at the leaf-level can be obtained using the BEPS-simulated leaf-level photosynthesis rate. In this way, the photosynthesis module of the BEPS and the fluorescence-photosynthesis model in the SCOPE model are incorporated.

Since the fluorescence emission efficiency is directly proportional to the fluorescence yield, multiplying APAR and Φ_F can be seen as an equivalent of leaf fluorescence (Lee et al., 2015). Considering that the total canopy is separated into sunlit and shaded leaves in the BEPS, the emitted fluorescence for the sunlit- and shaded-leaf groups were respectively generated in our study:

$$F_{su} = APAR_{su} \cdot \Phi_{Fsu} \tag{17}$$

$$F_{sh} = APAR_{sh} \cdot \Phi_{Fsh} \tag{18}$$

where su and sh represent the sunlit and shaded leaves, respectively.

3.3.2. Upscaling fluorescence from leaf to canopy

In the SCOPE model, the TOC SIF is simulated by modeling the fluorescence radiative transfer process in a multilayer canopy (60-layer) as a function of the solar zenith angle and leaf orientation (van der Tol et al., 2009). Since a complete run of this multilayer canopy radiative transfer model is too computationally expensive and not suitable for regional and global simulations. In a recent study conducted by Qiu et al. (2019), a simplified canopy fluorescence model was introduced to characterize the extinction and scattering effects of both sunlit and shaded leaves in the two-leaf based BEPS model. As described by Qiu et al. (2019), the fluorescence flux at canopy scale was separated as those came from sunlit and shaded leaves, which could be generated using simplified radiative transfer processes that consider canopy extinction and scattering for both sunlit and shaded leaf groups. After obtaining canopy fluorescence flux, Qiu et al. (2019) deployed a conversion factor to derive directional- and wavelength-dependent TOC SIF that corresponded with the remotely sensed one. Specifically, the upscaling process from leaf to canopy scale was mainly determined by LAI and SZA in Qiu et al.'s research (2019). Considering there are also studies that highlight the impact of V_{cmax} (Lee et al., 2015; Raczka et al., 2019) and brown material (van der Tol et al., 2019) in the leaf to canopy fluorescence upscaling process, it is still necessary to assess the factors that mostly affect the fluorescence upscaling process from leaf to canopy for a two-leaf based model. In this study, we introduced a canopy-averaged leaf-level fluorescence to derive TOC SIF. The canopy-averaged leaf-level fluorescence accounts for the contributions of both the sunlit and shaded leaf groups. A series of sensitivity analyses were conducted to assess the factors affecting the leaf to canopy upscaling process, which may also serve for further scaling studies between leaf and canopy fluorescence.

We focus on the TOC SIF at 740 nm, which corresponds with the GOME-2 SIF product, and only the nadir viewing direction was considered as the effect of viewing geometries is reduced by performing monthly averaging across all angles (Norton et al., 2019; Li et al., 2018a). In our study, the canopy-averaged leaf-level fluorescence was defined as a weighted summation of the sunlit- and shaded-leaf emitted fluorescence:

$$F = (F_{sun} \cdot LAI_{sun} + F_{sh} \cdot LAI_{sh})/LAI \tag{19}$$

The TOC SIF at 740 nm in the vertical viewing direction was generated using:

$$F_{740} = k \cdot F \tag{20}$$

where k is the upscaling factor related to leaf scattering, canopy structure, incident-observation geometry, and wavelengths.

In our study, we run the SCOPE model under various situations to assess the factors that determine the upscaling factor k. Although the upscaling factor has been reported to be related to V_{cmax} (Lee et al., 2015; Raczka et al., 2019) or LAI (Qiu et al., 2019; Thum et al., 2017), we also consider incoming shortwave radiation (R_{in}), air temperature (T_a) and C_{ab} in this study as these variables have a key influence on the simulated canopy-level fluorescence (Verrelst et al., 2015). The ranges of the input variables used for the SCOPE simulation are listed in Table 2.

By running the SCOPE model with varying input parameters, both F_{740} and F were obtained. Then, the relationship between leaf and canopy fluorescence was investigated.

We found that the slope of the leaf-canopy fluorescence relationship is mainly affected by LAI (Fig. S2). By contrast, V_{cmax}, C_{ab}, R_{in} and T_a have little contributions on the variation of the slope. Apparently, R_{in} affects the intensities of both leaf and canopy fluorescence but has no obvious impact on their relationship. Both C_{ab} and T_a slightly affect leaf and canopy fluorescence, which may be attributed to their connections with APAR and NPQ, respectively.

As shown in Fig. 2, the relationship between the leaf and canopy fluorescence can be characterized as linear, and the slope of this linear relationship (k) can be determined by LAI (Fig. 2a). We derived k using an empirical exponential equation that is related to LAI (Fig. 2b) as:

$$k = -0.9507 + e^{0.1270 \cdot LAI} \tag{21}$$

It should be noted that all the simulations were conducted by assuming the leaf-inclination distribution factor (LIDF) was spherical (LIDFa = -0.35 and LIDFb = -0.15), which has been proven to be suitable for most types of forests and crops (Wang and Jarvis 1990).

3.4. SIF simulations and evaluations

We ran the BEPS-SCOPE coupling model at both site-scale and global-scale. The GOME-2 monthly SIF product was used to evaluate our simulations. For site-scale simulation, our model was run at hourly interval, while for global simulation, the running was conducted at 3-hourly intervals to reduce the computational complexity and improve the simulation efficiency. We also deployed the SCOPE model to assess

Table 2
Ranges of variables used for SCOPE running.

Variables	Values (min/max/interval)
V_{cmax} (μmol/m^2/s)	10/110/10
LAI	0.5/5.5/0.5
C_{ab} (μg/cm^2)	5/20/5, 20/70/10
R_{in} (W/m^2)	100/1200/100
Ta (°C)	-10/40/5

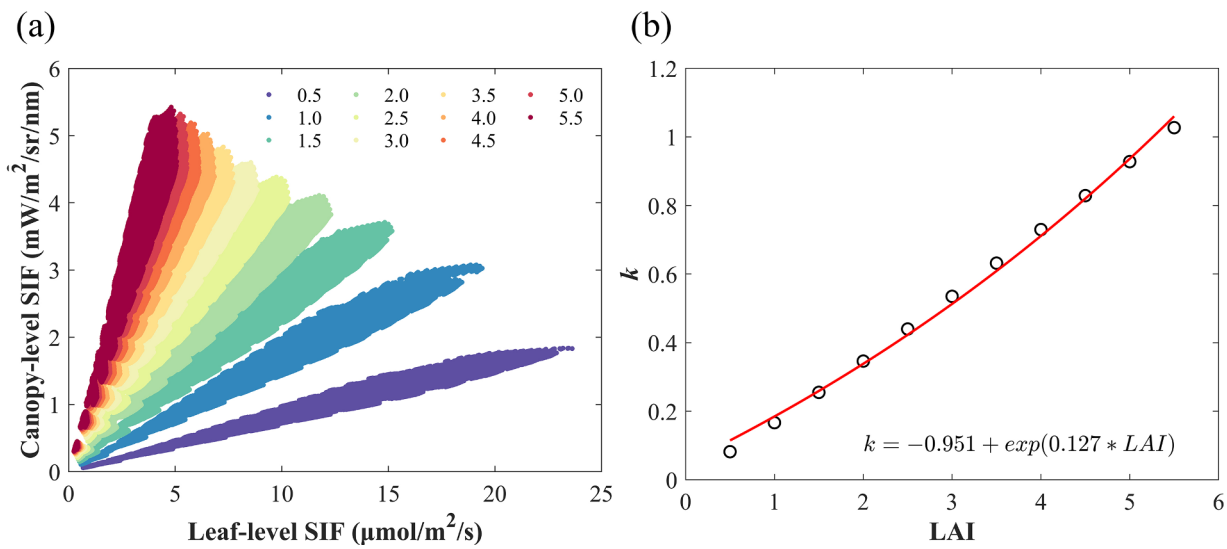

Fig. 2. The leaf-canopy fluorescence relationship under various LAI (a) and the relationship between k and LAI (b).

the performance of our model. To match with the GOME-2 monthly SIF product, all simulations were aggregated to a monthly scale.

In the photosynthesis module of BEPS, a PFT-specific canopy albedo was introduced to generate the leaf APAR. Considering that using a temporally consistent canopy albedo can inevitably lead to some uncertainties. For our site-scale simulation, we adopted the MODIS product for fraction of photosynthetically active radiation (FPAR) (MCD15A2H) (Myneni et al., 2015) to derive APAR. However, in our global-scale simulation, the PFT-specific canopy albedo was used to obtain APAR.

As SIF demonstrated a significant diurnal variation schema that corresponded with APAR (Cui et al., 2017; Liu et al., 2017a; Zhang et al., 2018a), the instantaneous daily SIF value at 9:30 am local time (LT), which is in consistent with the MetOp-A overpass time was obtained by calculating the averaged value of the retrievals of 9:00 am LT and 10:00 am LT or by interpolating the retrievals between 6:00 am LT and 12:00 am LT for the site-scale simulation and global simulation, respectively. Compared with the GOME-2 daily SIF product, the monthly SIF product excluded retrievals that were significantly contaminated by clouds (cloud fraction above 30%) (Joiner et al., 2013). Thus, we only considered the simulations under "clear-sky" conditions in generating monthly averaged SIF to match the GOME-2 monthly product. For our research, the clear-sky condition was defined as simulations when incoming shortwave radiation was above 80% of the monthly maximum incoming shortwave radiation. Likewise, the SCOPE based monthly SIF was also obtained using the "clear-sky" simulations.

To assess the performance of the BEPS-SCOPE coupling model, we adopt the coefficient of determination (R^2) and the root mean square error (RMSE) to quantify its ability in simulating SIF and GPP.

4. Results

4.1. Relationships between photochemistry, fluorescence, and heat dissipation

To assess our coupling framework, we explored the relationships between photochemistry, fluorescence, and heat dissipation using our model. By varying the incoming shortwave radiation, APAR, Φ_F, Φ_P, and k_N were obtained with our model. As shown in Fig. 3, the relationships between Φ_F, Φ_P, and k_N were found to be related with APAR. Specifically, Φ_F was positively related with k_N and negatively related with Φ_P when APAR was lower and turned to inverse relationships when APAR was higher. It suggested that our coupling framework can well characterize the relationships between Φ_F, Φ_P, and k_N under different APAR. According to the existing literature, under lower light conditions, more photosynthetic reaction centers are closed when APAR increases because the reduced quinone acceptor of PSII (Q_A) cannot be reoxidized in time (Baker, 2008), which results in a decreased Φ_P. In this case, since NPQ is inhibited by the proton gradient under low light intensity (Porcar-Castell et al., 2014), k_N increases slowly and Φ_F increases rapidly. Consequently, Φ_F is positively related with k_N and negatively related with Φ_P. By contrast, under higher light conditions, NPQ increases and dominates as protons are accumulated, thylakoid lumen pH is decreased when the light density increases, and both fluorescence and photochemistry are inhibited, resulting in a negative relationship between Φ_F and k_N and a positive relationship between Φ_F and Φ_P.

We also analyzed the temporal changes of k_N and Φ_P for all the selected sites. As the presented model deploys the sunlit-shaded leaf stratification strategy, we generated k_N and Φ_P for both sunlit (Figs. S3 and S4) and shaded leaf groups (Figs. S5 and S6) in this study. On a monthly scale, as shown in Figs. S3 and S5, k_N increases when APAR raises, while Φ_P decreases as APAR increases (Figs. S4 and S6). We found the seasonal changes of k_N and SIF seemed to change in opposite directions and tended to be negatively related (Figs. S3 and S5). Specifically, k_N demonstrates higher values in non-growing season and declines when SIF increases. During non-growing season, plants remain dormant, with lower temperature and less useful water inhibit photosynthesis, thereby resulting in a reduced Φ_P even under lower light conditions (Figs. S4 and S6). As photochemistry, NPQ, and fluorescence compete with each other, a reduced Φ_P leads to higher values of k_N. A further analysis on the seasonal dynamics of k_N for US-Ne1 (CRO), US-Ne2 (CRO), and US-Ne3 (CRO) indicated that C4 species exhibit higher k_N than C3 species, a result that was consistent with the observations conducted by Killi et al. (2017), suggesting a higher level of NPQ in the C4 species. We also noticed that the seasonal dynamics of k_N and Φ_P for evergreen species are smaller than those of deciduous species. A recent study conducted by Raczka et al. (2019) highlighted the necessity of separating k_N into sustained and reversible NPQ when modeling SIF for cold climate evergreen species, which lead to larger seasonal changes in k_N and SIF when compared to the fluorescence model used in our study. The method proposed by Raczka et al. (2019) can be adopted in further studies to test its applicability in various PFTs.

4.2. Site-scale SIF simulations

We tested the BEPS-SCOPE coupling model at site-scale. The comparisons among BEPS-SCOPE based, SCOPE based and GOME-2 SIF for

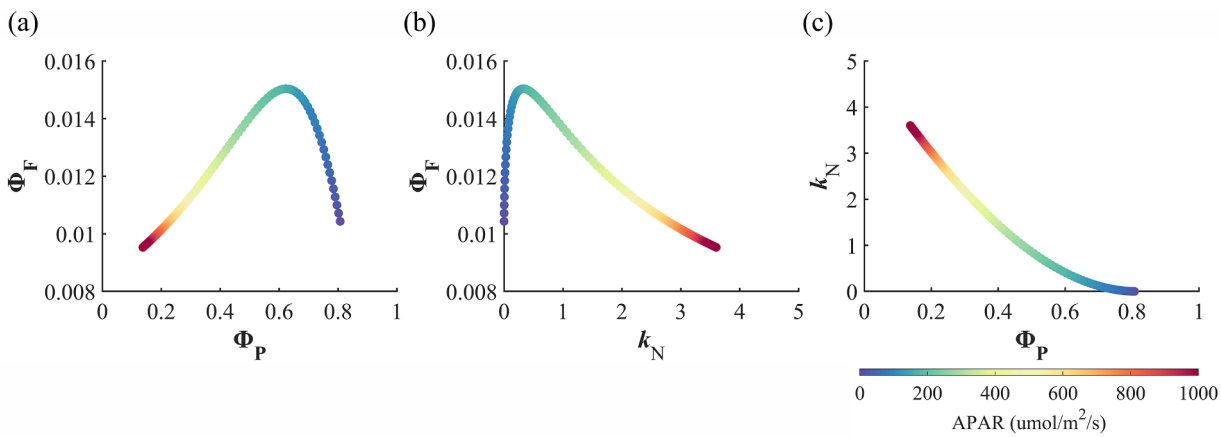

Fig. 3. Relationships between Φ_F, Φ_P, and k_N under various APAR.

four cropland sites (DE-Geb, US-Ne1, US-Ne2, US-Ne3) are presented in Fig. 4. We found that the monthly SIF simulated by BEPS-SCOPE were well correlated with the GOME-2 SIF product for all cropland sites ($R^2 > 0.92$, RMSE < 0.20 mW/m^2/sr/nm). Among these sites, DE-Geb was dominated by winter wheat (Revill et al., 2013), US-Ne1 was planted with maize. For US-Ne2 and US-Ne3, maize and soybean were planted as a rotation system. Specifically, US-Ne2 was planted with maize with the exception of 2008, and US-Ne3 was characterized by maize in odd years and turned to soybean in even years (Suyker et al., 2005). As winter wheat and soybean exhibit the C3 photosynthetic pathway and maize exploits the C4 photosynthetic pathway, we considered that our model can generate TOC SIF properly for both C3 and C4 species. The result was also consistent with earlier studies conducted by Zhang et al. (2014), van der Tol et al. (2014) and Guan et al. (2016). In these studies, the relationship between fluorescence and actual electron-transport rate was similar for both C3 and C4 species, which suggested our coupling schema in the model was irrelevant to photosynthesis type.

We also noted that the monthly SIF simulated by BEPS-SCOPE and SCOPE demonstrate similar distributions and contiguous numerical values (Fig. S7). However, the SCOPE based SIF was slightly higher than the BEPS-SCOPE based one, especially at the beginning and ending of growing season. This might be attributed to the constant leaf optical parameters used in our SCOPE simulation. In this study, we deployed PFT-specific C_{ab} and C_{ca} (carotenoid content) and assumed they remained constant. We also adopted constant values for C_w (leaf water equivalent layer), C_{dm} (dry matter content), and C_s (brown pigment fraction). These leaf optical parameters, however, have been proven to vary over time, especially for C_{ab} that affects both the absorption of photons and the production of fluorescence, which may result in some deviations. Compared with the SCOPE model, the BEPS-SCOPE has no module to deal with leaf optical characteristics and adopts a PFT-specific canopy albedo to generate APAR. We adopted the MODIS product for FPAR in generating leaf APAR in the BEPS-SCOPE, which may capture the seasonal variations of SIF more properly.

The monthly SIF values for five types of forests (DBF, EBF, DNF, ENF, and MF) simulated with our coupling model were also compared with those of the SCOPE based SIF and the GOME-2 SIF product (Fig. 5). In general, our simulated SIF was in close agreement with the SCOPE based one (Fig. S7). When compared with the GOME-2 SIF product, our model exhibited different performances for different forest types. For US-MMS and BE-Vie, which were planted with DBF and MF, respectively, the modeled and GOME-2 based SIF values were highly correlated ($R^2 > 0.80$, RMSE < 0.26 mW/m^2/sr/nm). However, the modeled SIF were significantly higher than the GOME-2 SIF values at both RU-SkP and US-Me2, which were characterized by DNF and ENF, respectively.

The deviations in simulating needleleaf species might be attributed to the radiative transfer theory used in the presented model. For broadleaf species, the thickness of the broadleaf is much smaller than the leaf width. The light transmitted through leaf edges is negligible compared to that exits the leaf outer layers. Compared with broadleaf species, needleleaf species are generally narrow and thick. Although needleleaf length can be assumed to be infinite relative to the leaf thickness and width, the leaf width can significantly affect leaf reflectance and transmittance. As leaf width is close to leaf thickness for most needleleaf species, the amount of light that escapes from needleleaf edge cannot be neglected. In our study, the radiative transfer theory of the SCOPE model was reduced into simple equations to improve the computational efficiency of the BEPS-SCOPE integrated model. The SCOPE model deploys the Fluspect theory in modeling leaf fluorescence, reflectance and transmittance. As Fluspect is established based on the PROSPECT model that is particularly suitable for broadleaf species, it may not be adequate to quantify the optical properties of needleleaf species due to "edge effects" (Zhang et al., 2008). Moreover, needleleaf species generally exhibit a complex canopy structure which demonstrate high clumping at both shoot and crown level (Rochdi et al., 2006), using the same setups as broadleaf species may lead to some deviations. Additionally, the semiempirical fluorescence-photosynthesis relating theory (van der Tol et al., 2014) deployed in our model was established without considering needleleaf species. The applicability of this theory to needleleaf species still requires further experiments and validation (van der Tol et al., 2019).

We also noted that the SIF values for the AU-Tum site (EBF) were overestimated when compared with the GOME-2 based SIF. This site is located in a warm temperate, fully humid area with a warm summer climate (Köppen climate classification Cfb) (Leuning et al., 2005). It occupies abundant precipitation throughout the year, which makes the area around the site more likely be contaminated by clouds. Although the monthly GOME-2 SIF product filters the retrievals when cloud fractions are above 30%, clouds are present in nearly every observation of GOME-2's large footprint (Joiner et al., 2013). By contrast, in our site-scale simulation, we first used a temporal gap-filling algorithm to derive continuous LAI values using clear-state retrievals. Then, a monthly averaging performance was conducted using only simulations under clear-sky conditions. These processes could handle the cloud-contaminated data more properly, which resulted in mismatches between the GOME-2 SIF values and simulated SIF values.

For the ZA-Kru site covered mainly by savanna, both the BEPS-SCOPE coupling model simulated and the SCOPE model simulated SIF were overestimated when compared with the GOME-2 SIF product (Fig. 6). We also noticed the simulated SIF has a systematic bias and exhibits double-peak in the seasonal cycle. This site is located on a broad-leaved and fine-leaved ecotone between *Combretum* savanna and

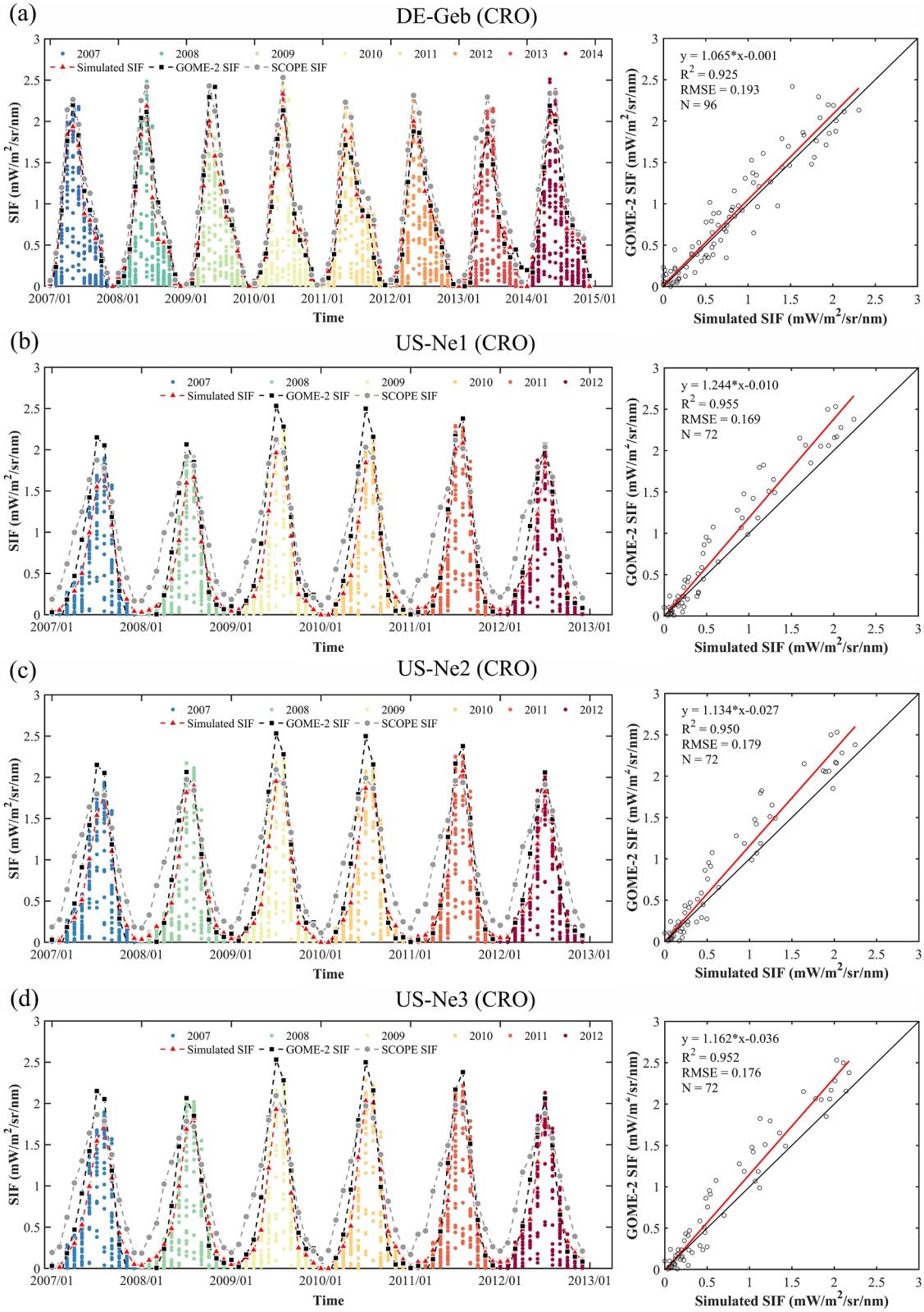

Fig. 4. Comparisons among our simulated SIF, SCOPE SIF, and the GOME-2 SIF product for four cropland sites. DE-Geb (a), US-Ne1 (b), US-Ne2 (c), US-Ne3 (d). The individual points in the left subplots represent the simulated SIF values at 9:30 am LT for each day. The monthly SIF were generated using only "clear-sky" simulations.

Acacia savanna planted on sandy soil and clayey soil, respectively. Various plants, including trees, shrubs, and grasslands, are distributed in a 300 m × 300 m area around the tower site (Scholes et al., 2001). In this case, we assumed the simulated SIF may deviate when using one set of parameters that were applicable for savanna. According to the MODIS product for land-cover types (MCD12Q1), 94.90%, 2.49%, 1.51%, 0.57%, and 0.53% of pixels within the GOME-2 grid cell belong to savanna, cropland, closed shrubland, open shrubland and urban and

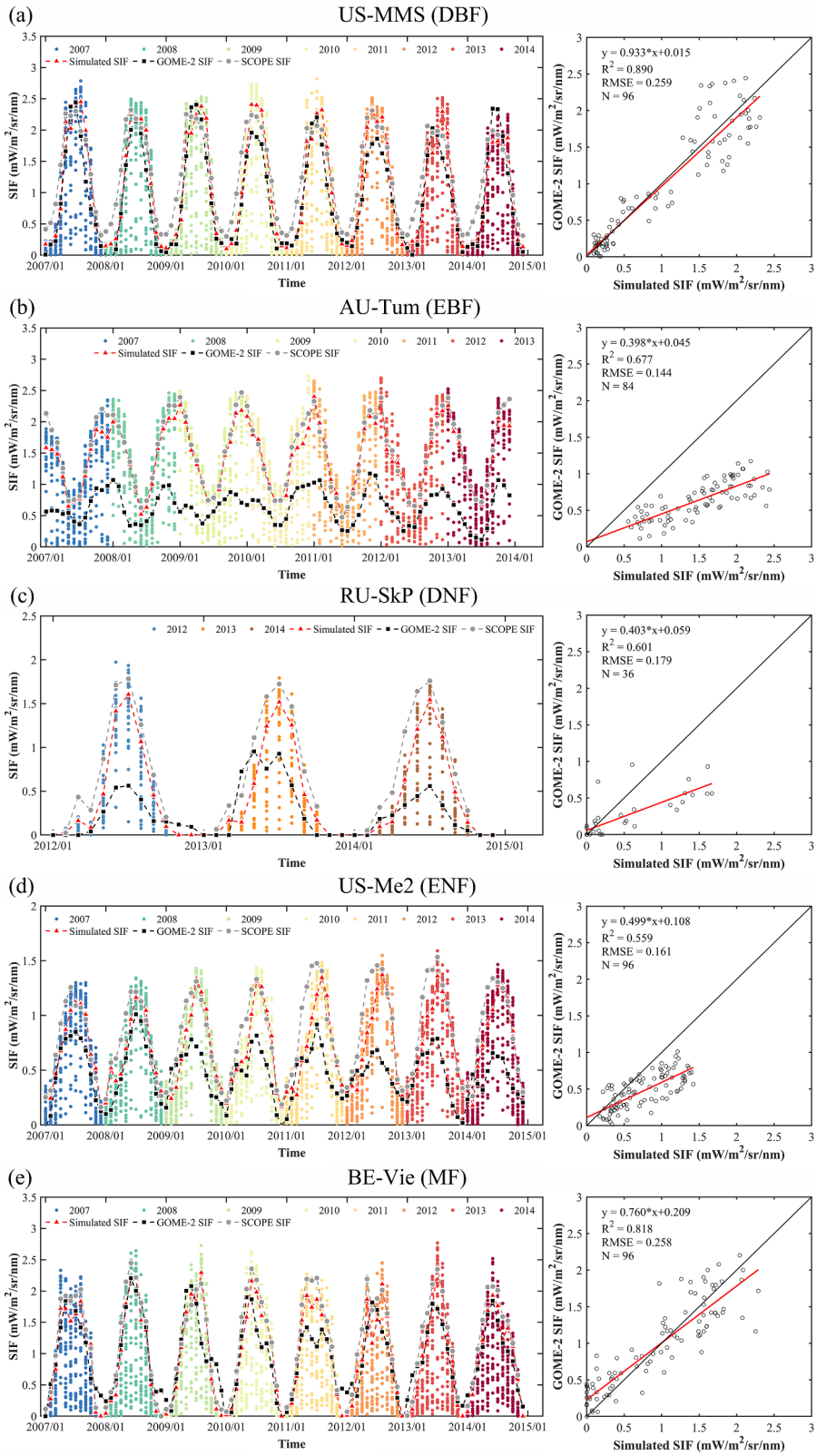

Fig. 5. Comparisons among our simulated SIF, SCOPE SIF, and the GOME-2 SIF product for five types of forest sites. US-MMS (a), AU-Tum (b), RU-SkP (c), US-Me2 (d), BE-Vie (e). The individual points in the left subplots represent the simulated SIF values at 9:30 am LT for each day. The monthly SIF were generated using only "clear-sky" simulations.

build-up, respectively. Except for the urban and build-up, we obtained the GLASS LAI and the MODIS FPAR for each land-cover and simulated monthly SIF using our coupling model. As shown in Fig. S8, the simulated monthly SIF for all land-cover types demonstrated double-peak in the seasonal cycle, which is consistent with the EC-based GPP. By contrast, the GOME-2 SIF product exhibited an earlier decline and showed a one-peak seasonality when compared with the EC-based GPP. Although a recent study reported that the TROPOMI SIF can well

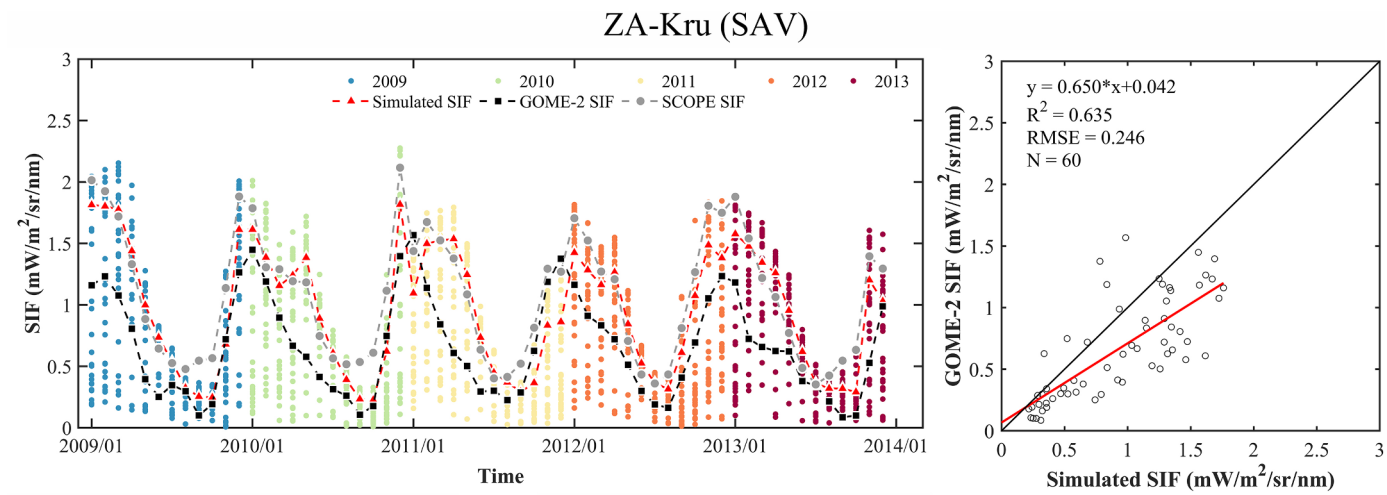

Fig. 6. Comparison among our simulated SIF, SCOPE SIF, and GOME-2 SIF product for the ZA-Kru site. The individual points in the left subplots represent the simulated SIF values at 9:30 am LT for each day. The monthly SIF were generated using only "clear-sky" simulations.

capture the double-peak seasonality of photosynthesis (Turner et al., 2020), monthly averaging of GOME-2 SIF likely masks out the higher frequency modes of variability. Additionally, the BEPS-SCOPE coupling model is applicable for structurally homogeneous canopies as the leaf to canopy upscaling factor is derived from the 1-D SCOPE model, there are some limitations when applied to complex canopies. This may be another reason for the deviations between the simulated and GOME-2 SIF.

4.3. Global SIF simulation

For global simulation, the coupling model was run at 3-hour intervals to reduce computational complexity and improve simulation efficiency. To match with the GOME-2 instantaneous monthly SIF data, we generated the daily instantaneous SIF values at 9:30 am LT by interpolating the retrievals between 6:00 am LT and 12:00 am LT. Consistent with the site-scale simulation, only the clear-sky daily SIF retrievals were used to obtain the instantaneous monthly averaged SIF.

The comparisons between the simulated SIF and GOME-2 SIF products in January, April, July and October 2012 are shown in Fig. 7 (globally distributed monthly SIF values throughout the year are provided in Fig. S9). We found that the simulated and GOME-2 SIF values were spatially and temporally well correlated. However, the simulated SIF demonstrated significant deviations in areas that were mainly covered with needleleaf canopies (black rectangles in Fig. 7). This finding was consistent with that of the site-scale simulation and reconfirmed that our model was limited when applied to the needleleaf land-use type. We also observed that the simulated SIF in tropical rainforest regions distributed near the equator were overestimated in comparison with the GOME-2 SIF. Due to the continuous periods of overcast sky or rainy weather in this region, the observations in the large footprints of GOME-2 were generally contaminated by clouds. Although the monthly SIF product excludes the retrievals with cloud fractions above 30%, the influence of cloud cannot be neglected in GOME-2's large footprint (Joiner et al., 2013). In contrast, the 0.05° GLASS LAI were first processed to exclude the retrievals that were influenced by clouds and then aggregated to a 0.5° resolution. These processes, in addition to the "clear-sky" aggregation method, significantly reduced the cloud contamination in a 0.5° × 0.5° grid. In addition, Fig. 7 also indicated that the modeled SIF generally overestimated in high-latitude regions in the northern hemisphere, a result that could be attributed to the satellite's overpass time used in our research. As the satellite's overpass time represents the local crossing time of the ascending node and only applies to the equator, high latitudes may have some differences. At high latitudes regions in the northern hemisphere, the irradiance may be lower than that at 9:30 am LT, which may lead to some deviations as SIF is very sensitive to APAR in the SIF-TBMs (Parazoo et al., 2020).

It should also be noted that the GOME-2 SIF was inherently noisy due to the instrument's low signal levels, especially for high-latitude regions (Joiner et al., 2013). In addition, the large area in South America (red rectangles in Fig. 7), known as the South Atlantic Anomaly (SAA), also demonstrated a high variability in the product as the performance of the instrument degraded in this region (Joiner et al., 2013). These inherent drawbacks of the GOME-2 SIF product also led to some mismatches in our evaluation.

To quantitatively assess the performance of our presented model, the relationship between the simulated monthly SIF and the GOME-2 based SIF was analyzed. As our model cannot well handle needleleaf species, the ENF and DNF data were excluded. As shown in Fig. 8, there were high correlations between these two SIF datasets for all monthly retrievals ($R^2 > 0.5$; RMSE < 0.36 mW/m^2/sr/nm). Compared with the simulated SIF, the GOME-2 SIF product demonstrated some high values during the late autumn and winter periods (black ellipses in Fig. 8). A further detailed analysis indicated that these high values were mainly distributed in Antarctica that was scarcely covered with vegetation, suggesting that some uncertainties still existed in the GOME-2 SIF product. Although the simulated SIF and the GOME-2 SIF were highly correlated, we also noticed that the simulated SIF was generally overestimated. This derivation could be partly attributed to cloud contamination within the GOME-2 footprint (Joiner et al., 2013). Additionally, the homogeneous assumption of our coupling model might have been violated within a 0.5° × 0.5° grid, which could have resulted in its decreased performance.

As the MetOp-A overpass time of 9:30 am is not appliable across the globe, we generated daily-averaged SIF using the simulated instantaneous SIF at 9:30 am LT and SZA following the method described in Frankenberg (2015) to eliminate the deviations caused by satellite's overpass time and illumination. The comparisons between simulated daily-averaged SIF and GOME-2 daily-averaged SIF at a monthly scale indicated that both SIF values were spatially and temporally well correlated (Fig. S10). Compared with the instantaneous monthly SIF, the deviations at high latitudes decrease significantly and the correlations between the two SIF datasets increases after performing a daily correction (Fig. S11).

4.4. GPP simulation

We also checked our coupling framework by evaluating its

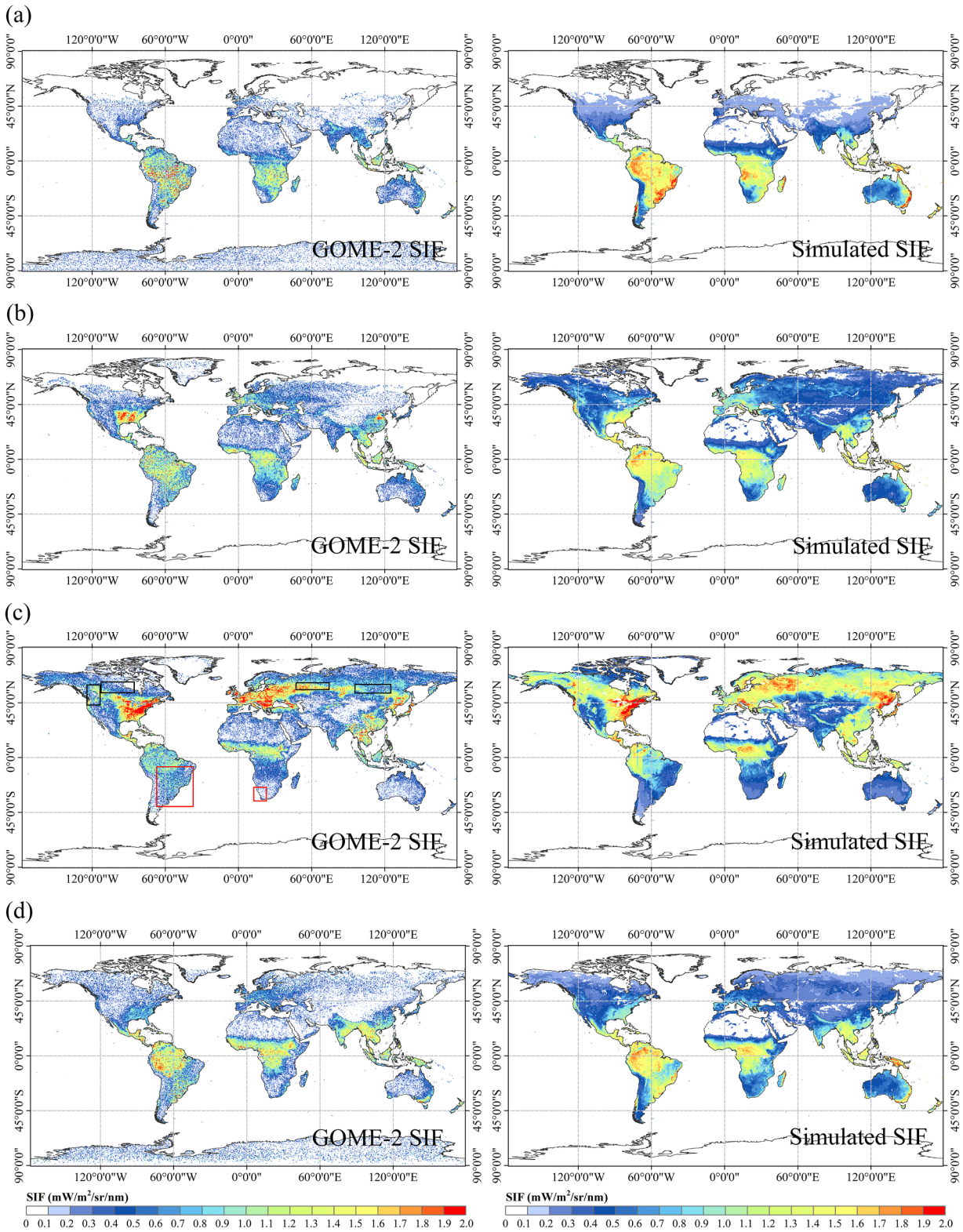

Fig. 7. Globally distributed GOME-2 SIF and simulated SIF for January (a), April (b), July (c), and October (d).

performance in simulating GPP. A comparison between the modeled monthly averaged daily GPP and the FLUXNET GPP was conducted. To generate monthly GPP, daily GPP was first obtained by aggregating the modeled hourly value to a daily scale, and the monthly averaged daily GPP was then generated using the mean value of the daily GPP for each month. As shown in Fig. 9, the simulated GPP was generally consistent with the FLUXNET GPP for all sites. We also found that the simulated GPP demonstrated overestimations when compared with EC-based GPP. A further detailed analysis indicated that the overestimation of GPP was mainly distributed at both the beginning and end dates of the growing period (Fig. S13). This kind of mismatch may be caused by parametric uncertainties in the model. As the coupling model simulates the eco-physiological, biogeochemical and the associated processes, numerous model parameters should be determined before running. Some

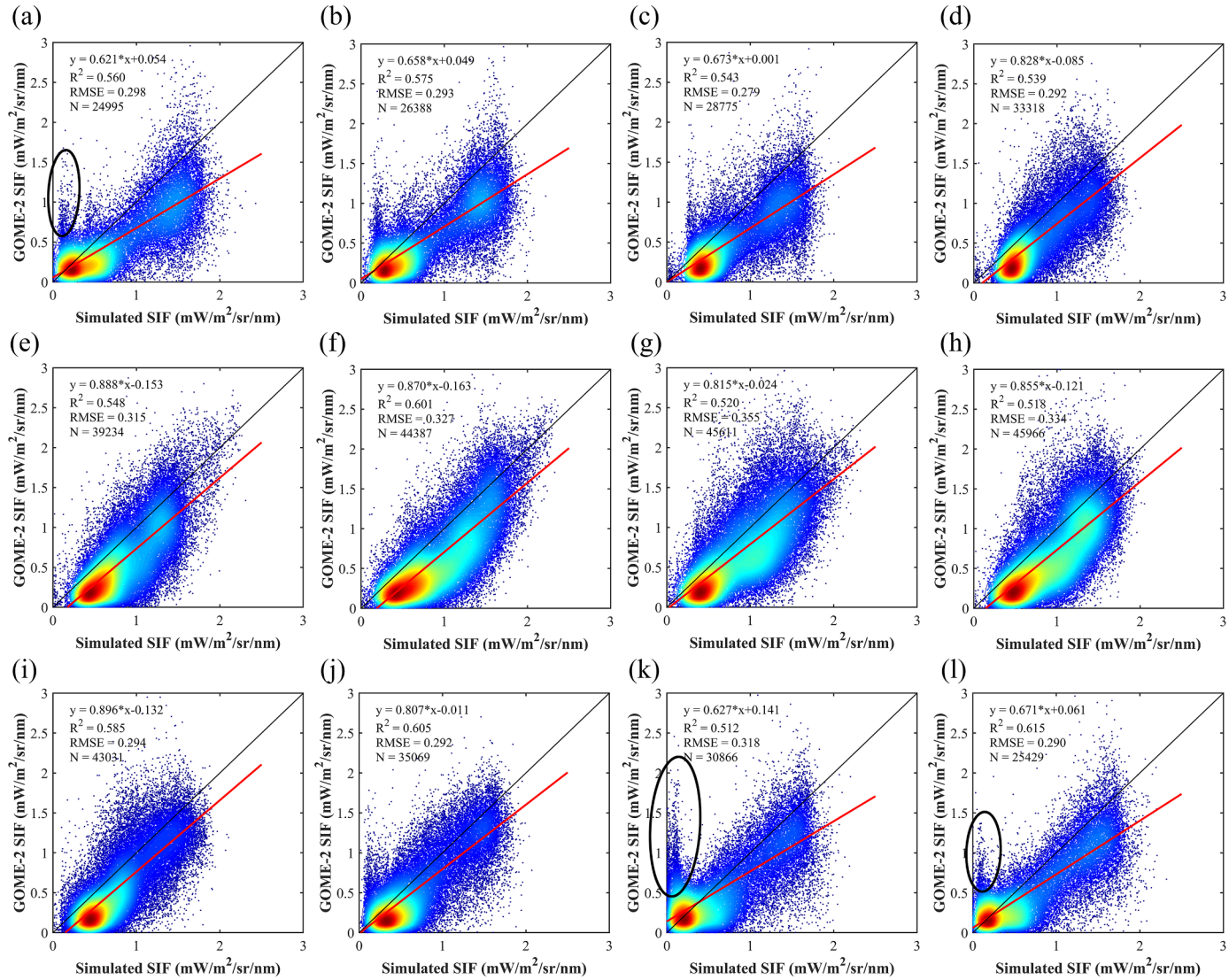

Fig. 8. Comparisons between the modeled SIF and the GOME-2 based SIF for January (a), February (b), March (c), April (d), May (e), June (f), July (g), August (h), September (i), October (j), November (k), and December (j).

important parameters, including V_{cmax} and the slope of stomatal conductance to the net photosynthetic rate (m), vary temporally (Houborg et al., 2013; Kosugi and Matsuo, 2006; Mo et al., 2008; Zhang et al., 2014). However, their values were treated as PFT-specific in our study, which may lead to some deviations.

We also compared our modeled GPP with the SCOPE based one. The instantaneous photosynthetic rates for both models at 9:30 am LT were generated. We found that our modeled GPP was well correlated with the SCOPE based one (Fig. S12). These comparisons confirm that the BEPS-SCOPE coupling model can properly integrate the photosynthetic theory of the two-leaf based BEPS and the fluorescence model of SCOPE and provide reasonable estimations for both SIF and GPP.

5. Discussion

5.1. Applied limitation of the BEPS-SCOPE coupling model

The integration of BEPS and SCOPE enabled the efficient generation of spatially distributed SIF and GPP. It provided additional outputs of TOC SIF at 740 nm that corresponded to the GOME-2 SIF product when compared with the outputs of the original version of BEPS. The model also simplified the radiative transfer physics of the SCOPE model and included a consideration of soil water effects. Thus, the presented model provided an efficient solution for regional/global SIF and GPP simulations.

Our integrated model introduced a simple equation (Eq. (17)) to simplify the fluorescence radiative transfer process within the canopy. This simplification was adopted from the SCOPE model in which a Fluspect model was used to characterize the reflectance, transmittance and fluorescence emissions of leaves and a FluorSAIL model was adopted to simulate the radiative transfer process within a multilayer canopy. As an extension of the classic broadleaf radiative transfer model PROSPECT, the Fluspect model may demonstrate some uncertainties in simulating the optical properties for needleleaf species that are small, narrow and irregularly shaped since the assumption of infinite plane layers for broadleaves is violated (Zhang, 2011; Zhang et al., 2008). Moreover, needleleaf species generally occupies strong clumping in both shoots and crowns, which enhancing the mutual shading between needles and affecting the radiant transfer process, thereby resulting in a lower reflectance when compared with broadleaf species (Rochdi et al., 2006). Likewise, the modeled SIF may demonstrate an overestimation for needleleaf species when compared with the remotely sensed one if we use the same setups as broadleaf species. In future studies, a correction factor for needleleaf species can be applied

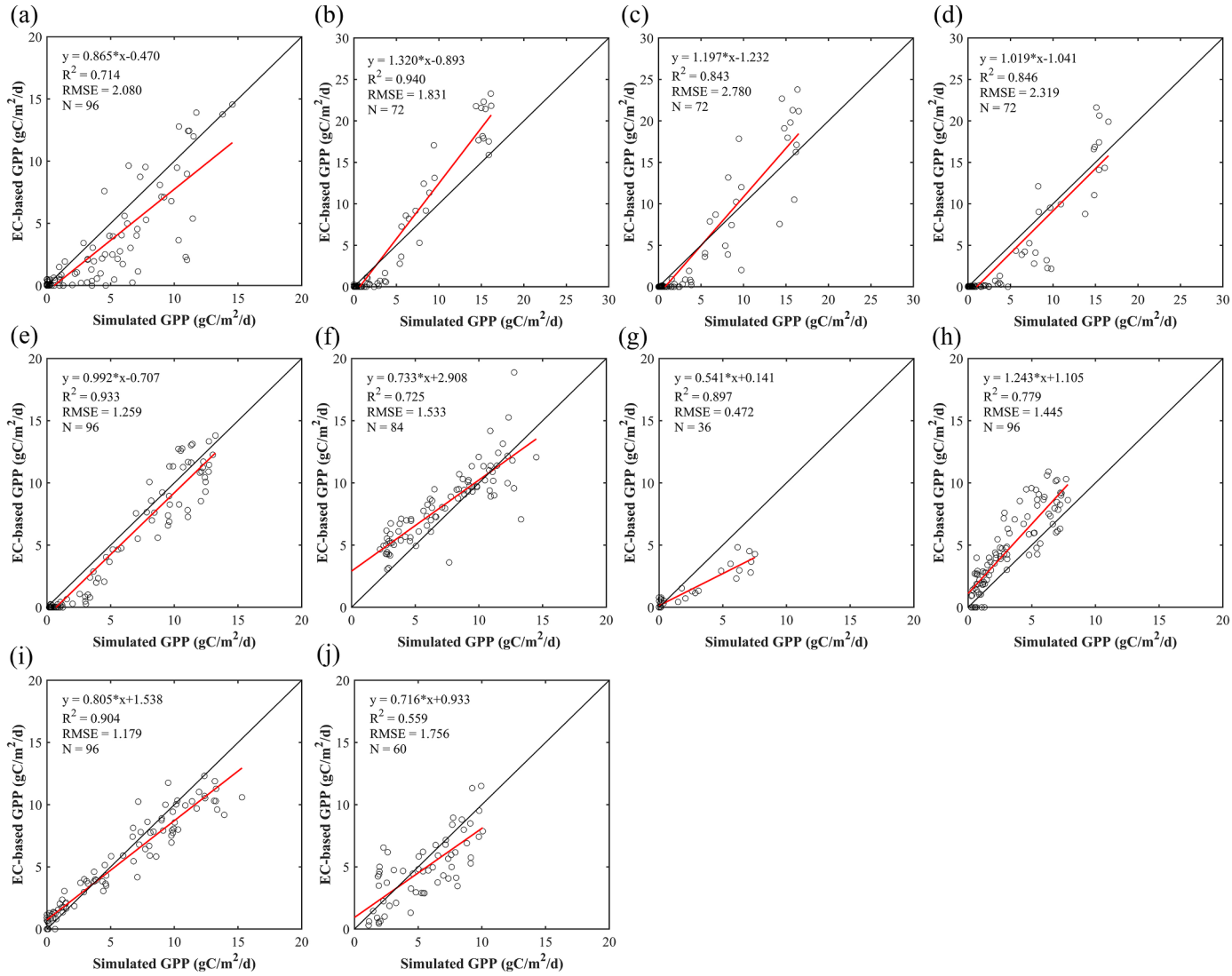

Fig. 9. Comparisons between the simulated GPP and the EC-based GPP for DE-Geb (a), US-Ne1 (b), US-Ne2 (c), US-Ne3 (d), US-MMS (e), AU-Tum (f), RU-SkP (g), US-Me2 (h), BE-Vie (i), and ZA-Kru (j).

to tackle these limitations. In addition, the FluorSAIL model, which was established based on the SAIL theory, is applicable for structurally homogeneous canopies. Terrestrial surface, however, are usually significantly heterogeneous, especially in large areas like the GOME-2 footprint. Therefore, more advanced models that can handle heterogeneous canopies should be considered when characterizing the radiative transfer of fluorescence.

In a study conducted by Zhao et al. (2016), a Monte Carlo ray-tracing model, FluorWPS (Fluorescence model with Weighted Photon Spread method) was proposed to deal with the fluorescence radiative transfer for heterogeneous 3-D canopies. Liu et al. (2019) modeled TOC SIF for heterogeneous forests using the Discrete Anisotropic Radiative Transfer (DART) model. These studies put forward solutions for simulating heterogeneous TOC SIF. However, the computation efficiency of FluorWPS or DART is relatively low, which may not be suitable for regional and global simulations. Thus, further studies are still needed to develop models that can coordinate accuracy, efficiency and applicability at various spatial scales.

We simulated TOC SIF at 740 nm in the vertical viewing direction for a comparison with the GOME-2 monthly SIF product. Although the impact of viewing geometry decreases after performing monthly averages, the instantaneous SIF demonstrate directional variations (Liu et al., 2016b; Van Wittenberghe et al., 2015). Thus, the proposed leaf-canopy fluorescence upscaling strategy in this study is limited in fully characterizing the optical properties of the TOC SIF, especially when compared with the instantaneous GOME-2 retrievals, further studies are still needed to model the bidirectional TOC SIF emissions for applications in more situations. Besides that, in a study conducted by Liu et al. (2016b), the bidirectional variation of TOC SIF was corrected to nadir using a semiempirical bidirectional reflectance distribution function (BRDF) model. A similar approach was performed by He et al. (2017) in order to derive hot spot directional TOC SIF using the GOME-2 SIF product. The findings of these studies indicated that the bidirectional TOC SIF can be angular normalized using the BRDF model or a hot spot function, which can extend the applicability of our model.

5.2. Uncertainties in the model parameters setting

Due to the fact that the SIF-GPP relationship is affected by light conditions, we adopted the BEPS model that follows the sunlit-shaded leaf stratification strategy (Liu et al., 1997; Norman, 1982; Wang and Leuning, 1998) in modeling canopy-level photosynthesis and fluorescence. In comparison to the big-leaf model, the two-leaf model has been proven to more efficiently handle the nonlinear response of leaf photosynthesis to meteorological variables (Chen et al., 1999; Zhang et al.,

2012). In this context, we expected that the BEPS-SCOPE coupling model can effectively and efficiently simulate the fluorescence emissions, a parameter that is correlated with photosynthesis (Eq. (7)). However, a recent study conducted by Parazoo et al. (2020) suggested that the simulated APAR shows significant variations across different SIF-TBMs. Although our simulated SIF and GPP were generally consistent with the SCOPE based ones at site-scale, the fundamental methods in generating sunlit/shaded LAI and APAR are different across these two models. The BEPS-SCOPE coupling model adopts the empirical formula of Erbs et al. (1982) and Black et al. (1991) to derive direct and diffuse irradiances above canopy, it also deploys the methods of Norman (1982) and Chen et al. (1999) in obtaining LAI and PAR for sunlit and shaded leaf groups. The sunlit/shaded APAR is then calculated using PAR and PFT-specific canopy albedo. By contrast, the SCOPE model deploys a semi-analytical radiative transfer approach in generating sunlit/shaded LAI and APAR in a 60-layer canopy by considering the impact of both leaf optical properties and canopy structure. It distinguishes the shaded leaves into 60 elements (60 layers) and treats the sunlit leaves as 60 × 13 × 36 elements (60 layers, 13 leaf inclinations, and 36 leaf azimuth angles) in deriving the interceptions of solar fluxes for sunlit and shaded leaf groups (van der Tol, et al., 2009). In this study, we compared the BEPS-SCOPE simulated sunlit/shaded LAI and APAR with the SCOPE based ones. As the sunlit/shaded fractions are mainly determined by SZA in the BEPS-SCOPE coupling model (Norman, 1982; Chen et al., 1999), we derived sunlit/shaded LAI and APAR with BEPS-SCOPE and SCOPE by varying SZA from 0° to 60° with an interval of 10°, LAI from 1 to 5 with an interval of 1, and R_{in} from 100 W/m^2 to 1000 W/m^2 with an interval of 100 W/m^2. As shown in Fig. 10, the sunlit/shaded LAI simulated using both models are almost identical. We also noticed the sunlit APAR simulated by both models demonstrated high consistency while the shaded APAR exhibited significant differences between the two models. In our site-scale simulations, we adopted the MODIS FPAR in generating APAR for sunlit and shaded leaf groups, which lead to similar seasonal variation trends when compared with the GOME-2 SIF product. Deploying the MODIS FPAR product can reduce some uncertainties caused by the pre-defined PFT-specific canopy albedo in generating APAR, but it cannot avoid the uncertainties caused by model schema. In Parazoo et al.'s (2020) study, they highlighted that the SIF-TBMs based APAR generally deviate from the field measurements. As the relationship between Φ_P and Φ_F is different when APAR changes, more comprehensive evaluations and comparisons should be performed in future studies.

Although our coupling model performed well for most sites when performing monthly comparisons, some deviations still existed when we compared the interannual variations of the simulated SIF with the GOME-2 SIF product (Fig. S14). We found that the simulated SIF demonstrated overestimations when compared with the GOME-2 SIF product. Like the overestimation of GPP, the overestimation of annual SIF can be mainly attributed to the overestimated SIF values at both the beginning and end dates of the growing period (Figs. 4–6). We considered that the consistent temporal parameter settings in our simulation can lead to this type of deviation. In the research conducted by Zhang et al. (2014), Zhang et al. (2018c), Guan et al. (2016), and Camino et al. (2019), remotely sensed SIF was used to derive V_{cmax}. Additionally, SIF has been proven to be related to canopy conductance (Shan et al., 2019). Recent studies have also discussed the possibility of optimizing model parameters by assimilating the SIF data into the terrestrial biosphere models (Koffi et al., 2015; Norton et al., 2019; Dutta et al., 2019). These studies suggest that SIF has the potential to reduce model uncertainties through model parameterization, which supports further studies in accurately estimating regional and global GPP using our BEPS-SCOPE integrated model.

5.3. Limitations in upscaling SIF from leaf to canopy

In our study, the upscaling factor for SIF at 740 nm, which is located in the far-red region, was found to be mainly affected by LAI. In contrast, the red SIF was also affected by the reabsorption of leaf chlorophyll, especially when C_{ab} was below 30 μg/cm^2 (Fig. 11), which makes the relationship between leaf and canopy fluorescence more complex in this spectral range. Although Liu and Cheng (2010) and Liu et al. (2017b) suggested that far-red TOC SIF is more reliable for estimating GPP due to the chlorophyll reabsorption effect at red band, the red SIF has been proven to be more physiologically related to photosynthesis (Verrelst et al., 2016, Liu et al., 2020), which makes it essential for photosynthesis, especially in short-time scale studies. Thus, the simulation of red TOC SIF is as important as the far-red one.

We used an upscaling factor that is related to LAI to generate TOC SIF after conducting a series of sensitivity analyses. As the canopy-averaged leaf-level fluorescence was generated using fluorescence that comes from both sunlit and shaded leaves, we considered that the upscaling factor can account for the canopy extinction and scattering effects for both sunlit and shaded leaf groups. Although the proposed method greatly improved the efficiency of our simulation, it should be noted that recent literature highlights the influence of incident-observation geometry and brown pigments (C_s) in determining the canopy SIF escape probability (van der Tol et al., 2019). Thus, we investigate their impacts on the leaf to canopy upscaling process. Considering that R_{in} affects the intensities of both leaf and canopy fluorescence, it was also included to enlarge the ranges of the intensity values. The ranges of the input values used for the SCOPE simulation are listed in Table S2.

As shown in Fig. 12, apart from LAI, C_s also has an impact on the upscaling process. This impact can be attributed to the competition relationship between brown pigments and chlorophyll for their absorption of photons, which makes C_s affect the production of fluorescence. SZA affects the intensities of leaf and canopy fluorescence but only has slight impact on their relationship, while VZA shows no obvious influence on the upscaling factor. Compared with the results that

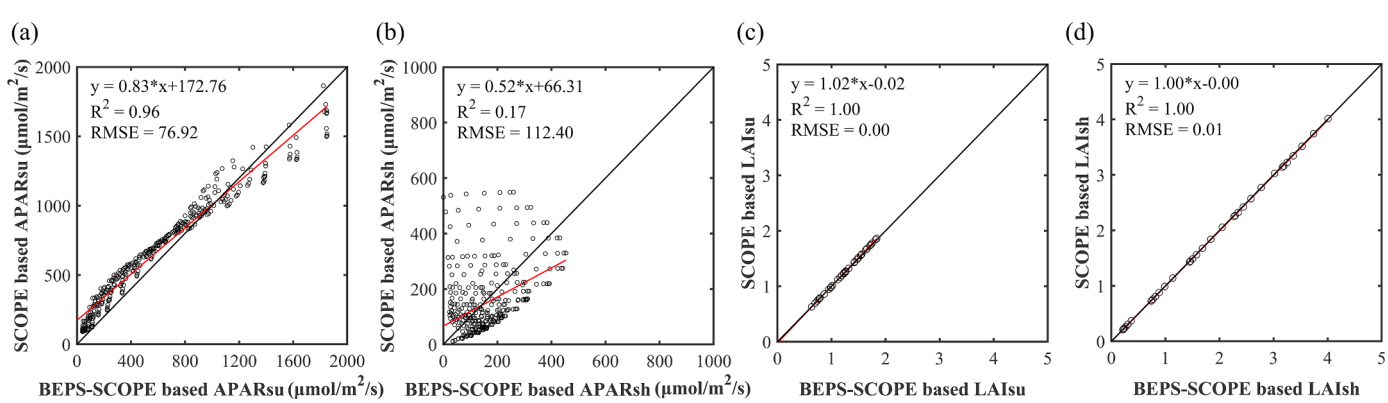

Fig. 10. Comparisons between BEPS-SCOPE based and SCOPE based APAR and LAI for sunlit and shaded leaf groups.

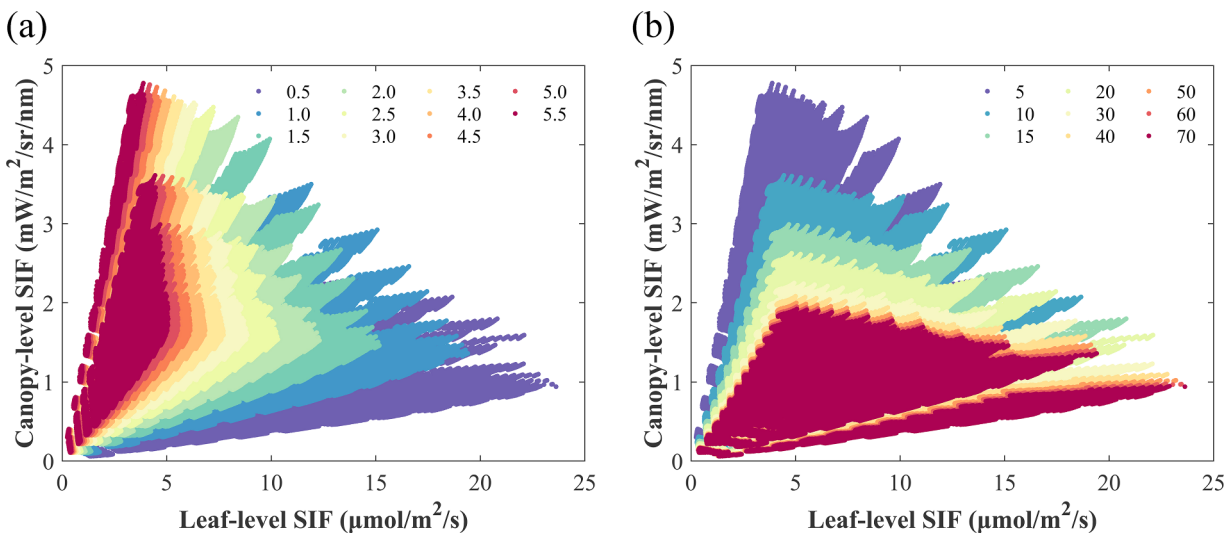

Fig. 11. The leaf-canopy fluorescence relationship at the red region (685 nm) under various LAI (a) and C_{ab} (unit: μg/cm^2) (b).

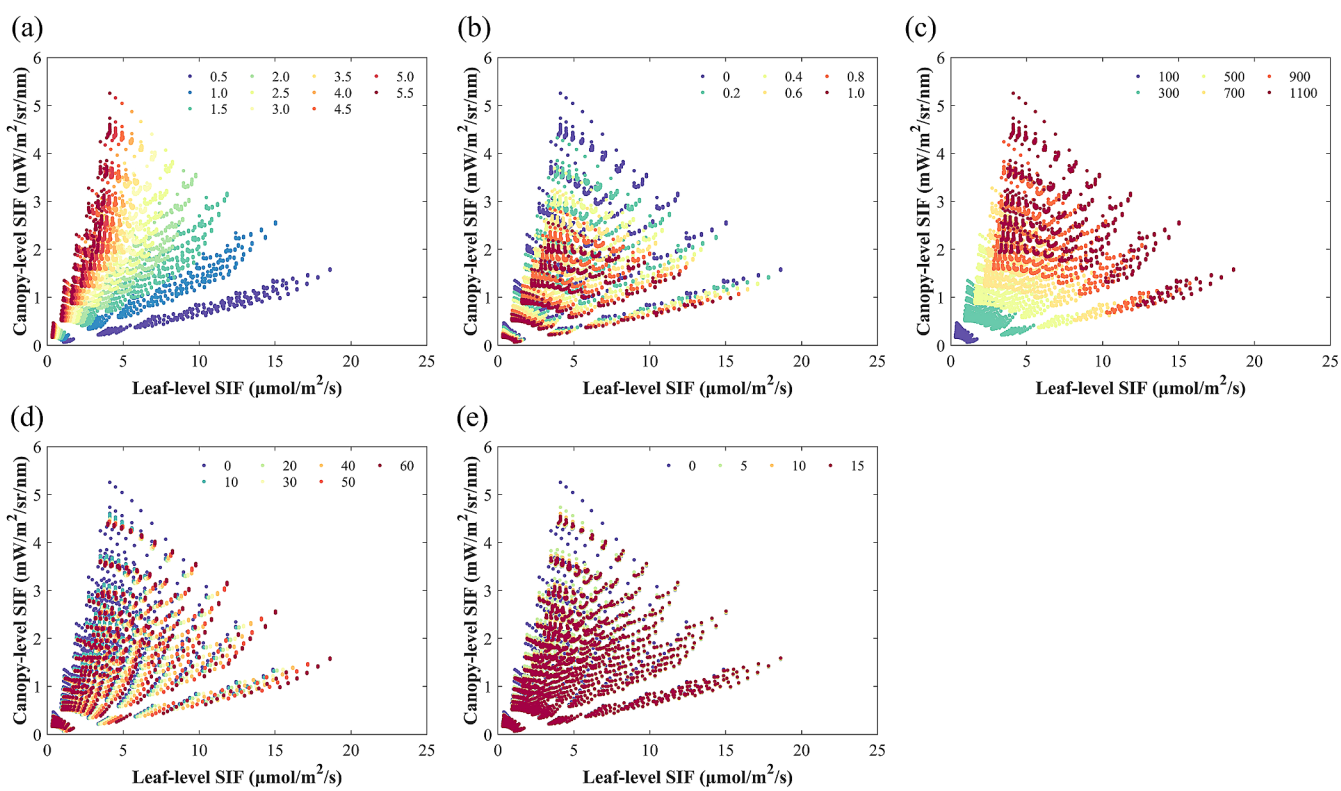

Fig. 12. The leaf-canopy fluorescence relationship under various LAI (a), C_s (unit: fraction) (b), R_{in} (unit: W/m^2) (c), SZA (°) (d), and VZA (°) (e).

neglect the influence of C_s (Fig. S2), the relationship between leaf and canopy fluorescence varies as R_{in} changes. As C_s affects the absorption of photons, increased C_s can lead to decreased absorption and fluorescence, leading to changeable relationship between leaf and canopy fluorescence changes even when R_{in} remain constant. However, a recent study conducted by Pacheco-Labrador et al. (2020) suggested that SCOPE may neglect the differences between green and senescent leaf groups in modeling radiative transfer and exchanges of heat, water and CO_2. The influence of C_s cannot be neglected and should be investigated in further studies using the senSCOPE model (Pacheco-Labrador et al., 2020) that is more suitable in modeling canopies with mixed green and senescent leaves.

In this study, we only considered the spherical leaf inclination angle distribution scenario in assessing the factors that affect the leaf to canopy upscaling process, which may lead to some considerable deviations as the angular distribution of leaves affects the allocation of incident radiations on sunlit and shaded leaf groups as well as the escape ratio of fluorescence. To assess the impacts of leaf inclination, six types of leaf inclination angle distributions including spherical, uniform, planophile, plagiophile, erectophile and extremophile (Goel, 1988) were tested. We found that although LAI mostly determine the relationship between leaf and canopy fluorescence for all types of leaf inclination angle distributions, the empirical relationships between the upscaling factor and LAI are different (Fig. 13). Thus, we advocate using biome-specific upscaling factors in the scaling research between leaf and canopy fluorescence.

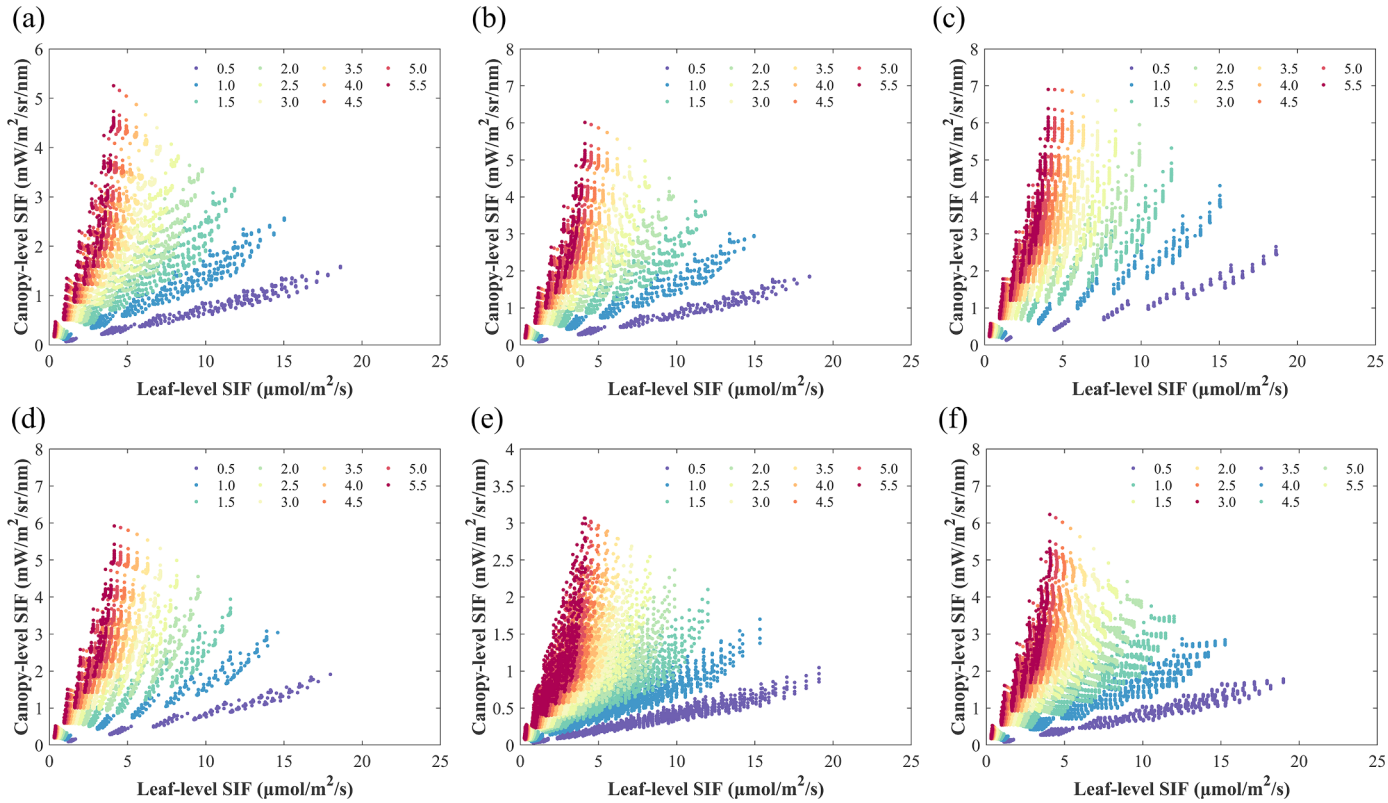

Fig. 13. The leaf-canopy fluorescence relationship under various LAI for spherical (a), uniform (b), planophile (c), plagiophile (d), erectophile (e), and extremophile (f) leaf inclination angle distributions.

In a recent study conducted by Liu et al. (2018a), a random forest model was proposed to downscale SIF from canopy-level to photosystem level, which facilitated the normalization of SIF observations across canopy types and incident-observation geometries. As machine learning or deep learning algorithms can deal with nonlinear relationships between leaf and canopy SIF, we expect it can be adopted in further studies to derive TOC SIF.

5.4. Uncertainties in the model evaluation

To match with the GOME-2's large footprint, we adopted EC flux sites that were spatially homogeneous over large areas to test our model. During the site-scale simulation, we employed the FLUXNET based meteorological data and the 1 km GLASS LAI, which are inconsistent with the GOME-2's footprint. Therefore, some uncertainties existed when using GOME-2 SIF to assess our site-scale simulation, especially for the ZA-Kru site (Fig. 6) which demonstrated a higher heterogeneity. Additionally, in our global scale simulation, the 0.05° GLASS LAI was spatially aggregated to a 0.5° spatial resolution after performing a temporal gap-filling algorithm to exclude LAI that were contaminated by clouds. We also adopted a "clear-sky" temporal SIF aggregation method to further reduce the influences of clouds. We expect these processes can derive more "clearer" SIF in a 0.5° × 0.5° grid than the monthly GOME-2 SIF product and can lead to some deviations. Fortunately, the spatial and temporal resolutions of remotely sensed SIF are expected to increase substantially in the near future. In comparison with GOME-2, the OCO-2 (Frankenberg et al., 2014), TROPOMI (Guanter et al., 2015; Köhler et al., 2018), Tansat (Du et al., 2018; Liu et al., 2018b) and ESA's Earth Explorer Fluorescence Explorer (FLEX) (Drusch et al., 2017) can provide finer resolution SIF retrievals that are less contaminated by clouds. Although both OCO-2 and Tansat based SIF are spatially and temporally discontinuous, some spatial-temporal downscaling approaches have been recently put forward to generate global spatially contiguous SIF data at relatively high spatial and temporal resolutions (Duveiller and Cescatti, 2016; Gentine and Alemohammad, 2018; Zhang et al., 2018a; Li and Xiao, 2019). The availability of these high-quality SIF can be adopted to test and evaluate our model at a finer resolution in future studies.

6. Conclusions

In this study, we proposed an integrated model that linked BEPS and SCOPE models to facilitate spatial SIF simulations for regional and global applications. The model deployed the sunlit-shaded leaf separation strategy, which made it possible to efficiently capture the nonlinear responses of water, heat, CO_2 fluxes and the associated fluorescence to environmental factors. Furthermore, the fluorescence radiative transfer process described in the SCOPE model was simplified to improve model efficiency. This BEPS-SCOPE coupling model has a high computational speed and precision, which makes it possible for use in regional and global SIF simulations.

We put forward a canopy-averaged leaf-level fluorescence to represent the fluorescence that comes from both sunlit and shaded leaves. The canopy-averaged leaf-level fluorescence is obtained by calculating the LAI weighted summation of the sunlit- and shaded-leaf emitted fluorescence. After performing a series of sensitivity analyses, we found that the relationship between leaf-level and canopy-level fluorescence at 740 nm was mainly affected by LAI, the impacts of V_{cmax}, C_{ab}, R_{in}, Ta, SZA and VZA were relatively small. Although brown pigments and leaf inclination angle demonstrated some impacts on the scaling process, we found that using an LAI-based equation can well characterize the fluorescence radiative transfer process within the canopy. This finding makes it possible to use simplified equations to describe the complex fluorescence radiative transfer process within the canopy, which promotes our model's efficiency.

Due to the inherent limitation of the radiative transfer theory used

in the coupling model, the current version of our model has some limitations when applied to needleleaf species. However, for most species, the model demonstrated a good performance in both site-scale and global-scale simulations, which suggests that it can be used for regional and global applications, especially as a prior constraint in a GPP estimation.

Declaration of Competing Interest

The authors declare that they have no known competing financial interests or personal relationships that could have appeared to influence the work reported in this paper.

Acknowledgement

This work was supported by the National Key R&D Program of China (2017YFA0603002), the National Natural Science Foundation of China (41531174), the Natural Science Foundation of Jiangsu Province (BK20190764), and the Open Fund of State Key Laboratory of Remote Sensing Science (OFSLRSS202005). We would like to thank Prof. Jingming Chen and Dr. Gang Mo from University of Toronto for providing the BEPS model. The data from FLUXNET 2015 dataset were used in this work, we sincerely thank all contributors of the data.

Supplementary materials

Supplementary material associated with this article can be found, in the online version, at doi:10.1016/j.agrformet.2020.108169.

References

Anthoni, P.M., Knohl, A., Rebmann, C., Freibauer, A., Mund, M., Ziegler, W., Kolle, O., Schulze, E.D., 2004. Forest and agricultural land-use-dependent CO_2 exchange in Thuringia, Germany. Glob. Change Biol. 10, 2005–2019.
Archibald, S.A., Kirton, A., van der Merwe, M.R., Scholes, R.J., Williams, C.A., Hanan, N., 2009. Drivers of inter-annual variability in Net Ecosystem Exchange in a semi-arid savanna ecosystem, South Africa. Biogeosciences 6, 251–266.
Aubinet, M., Chermanne, B., Vandenhaute, M., Longdoz, B., Yernaux, M., Laitat, E., 2001. Long term carbon dioxide exchange above a mixed forest in the Belgian Ardennes. Agric. For. Meteorol. 108, 293–315.
Bacour, C., Maignan, F., MacBean, N., Porcar-Castell, A., Flexas, J., Frankenberg, C., Peylin, P., Chevallier, F., Vuichard, N., Bastrikov, V., 2019. Improving estimates of gross primary productivity by assimilating solar-induced fluorescence satellite retrievals in a terrestrial biosphere model using a process-based SIF model. J. Geophys. Res. Biogeosci. 124, 3281–3306.
Baker, N.R., 2008. Chlorophyll fluorescence: a probe of photosynthesis in vivo. Annu. Rev. Plant Biol. 59, 89–113.
Baldocchi, D., Falge, E., Gu, L.H., Olson, R., Hollinger, D., Running, S., Anthoni, P., Bernhofer, C., Davis, K., Evans, R., Fuentes, J., Goldstein, A., Katul, G., Law, B., Lee, X.H., Malhi, Y., Meyers, T., Munger, W., Oechel, W., U, K.T.P., Pilegaard, K., Schmid, H.P., Valentini, R., Verma, S., Vesala, T., Wilson, K., Wofsy, S., 2001. FLUXNET: A new tool to study the temporal and spatial variability of ecosystem-scale carbon dioxide, water vapor, and energy flux densities. Bull. Amer. Meteorol. Soc. 82, 2415–2434.
Black, T.A., Chen, J.-M., Lee, X., Sagar, R.M., 1991. Characteristics of shortwave and longwave irradiances under a Douglas-fir forest stand. Canad. J. Forest Res. 21, 1020–1028.
Camino, C., Gonzalez-Dugo, V., Hernandez, P., Zarco-Tejada, P.J., 2019. Radiative transfer Vcmax estimation from hyperspectral imagery and SIF retrievals to assess photosynthetic performance in rainfed and irrigated plant phenotyping trials. Remote Sens. Environ. 231, 111186.
Campbell, J.L., Law, B.E., 2005. Forest soil respiration across three climatically distinct chronosequences in Oregon. Biogeochemistry 73, 109–125.
Chen, J., Liu, J., Cihlar, J., Goulden, M., 1999. Daily canopy photosynthesis model through temporal and spatial scaling for remote sensing applications. Ecol. Model. 124, 99–119.
Chen, J.M., Mo, G., Pisek, J., Liu, J., Deng, F., Ishizawa, M., Chan, D., 2012. Effects of foliage clumping on the estimation of global terrestrial gross primary productivity. Glob. Biogeochem. Cycle 26.
Collatz, G.J., Ribas-Carbo, M., Berry, J., 1992. Coupled photosynthesis-stomatal conductance model for leaves of C4 plants. Aust. J. Psychol. 19, 519–538.
Cui, T.X., Sun, R., Qiao, C., Zhang, Q., Yu, T., Liu, G., Liu, Z.G., 2017. Estimating Diurnal Courses of Gross Primary Production for Maize: A Comparison of Sun-Induced Chlorophyll Fluorescence, Light-Use Efficiency and Process-Based Models. Remote Sens. 9.
Damm, A., Guanter, L., Paul-Limoges, E., van der Tol, C., Hueni, A., Buchmann, N., Eugster, W., Ammann, C., Schaepman, M.E., 2015. Far-red sun-induced chlorophyll fluorescence shows ecosystem-specific relationships to gross primary production: An assessment based on observational and modeling approaches. Remote Sens. Environ. 166, 91–105.
De Pury, D., Farquhar, G., 1997. Simple scaling of photosynthesis from leaves to canopies without the errors of big-leaf models. Plant Cell Environ 20, 537–557.
Drusch, M., Moreno, J., Del Bello, U., Franco, R., Goulas, Y., Huth, A., Kraft, S., Middleton, E.M., Miglietta, F., Mohammed, G., 2017. The FLuorescence EXplorer Mission Concept—ESA's Earth Explorer 8. IEEE Trans. Geosci. Remote Sensing 55, 1273–1284.
Du, S., Liu, L., Liu, X., Zhang, X., Zhang, X., Bi, Y., Zhang, L., 2018. Retrieval of global terrestrial solar-induced chlorophyll fluorescence from TanSat satellite. Sci. Bull. 63, 1502–1512.
Dutta, D., Schimel, D.S., Sun, Y., van der Tol, C., Frankenberg, C., 2019. Optimal inverse estimation of ecosystem parameters from observations of carbon and energy fluxes. Biogeosciences 16, 77–103.
Duveiller, G., Cescatti, A., 2016. Spatially downscaling sun-induced chlorophyll fluorescence leads to an improved temporal correlation with gross primary productivity. Remote Sens. Environ. 182, 72–89.
Erbs, D., Klein, S., Duffie, J., 1982. Estimation of the diffuse radiation fraction for hourly, daily and monthly-average global radiation. Solar energy 28, 293–302.
Farquhar, G.v., von Caemmerer, S.v., Berry, J., 1980. A biochemical model of photosynthetic CO_2 assimilation in leaves of C3 species. Planta 149, 78–90.
Feng, X., Liu, G., Chen, J.M., Chen, M., Liu, J., Ju, W.M., Sun, R., Zhou, W., 2007. Net primary productivity of China's terrestrial ecosystems from a process model driven by remote sensing. J. Environ. Manage. 85, 563–573.
Flexas, J., Escalona, J.M., Evain, S., Gulias, J., Moya, I., Osmond, C.B., Medrano, H., 2002. Steady-state chlorophyll fluorescence (Fs) measurements as a tool to follow variations of net CO_2 assimilation and stomatal conductance during water-stress in C-3 plants. Physiol. Plant. 114, 231–240.
Frankenberg C.2015. Solar Induced Chlorophyll Fluorescence: OCO-2 Lite Files (B7000) User Guide. Technical Report, NASA Jet Propulsion Laboratory, California Institute of Technology.
Frankenberg, C., Fisher, J.B., Worden, J., Badgley, G., Saatchi, S.S., Lee, J.E., Toon, G.C., Butz, A., Jung, M., Kuze, A., Yokota, T., 2011. New global observations of the terrestrial carbon cycle from GOSAT: Patterns of plant fluorescence with gross primary productivity. Geophys. Res. Lett. 38, L17706.
Frankenberg, C., O'Dell, C., Berry, J., Guanter, L., Joiner, J., Köhler, P., Pollock, R., Taylor, T.E., 2014. Prospects for chlorophyll fluorescence remote sensing from the Orbiting Carbon Observatory-2. Remote Sens. Environ. 147, 1–12.
Friedl, M.A., Sulla-Menashe, D., Tan, B., Schneider, A., Ramankutty, N., Sibley, A., Huang, X.M., 2010. MODIS Collection 5 global land cover: Algorithm refinements and characterization of new datasets. Remote Sens. Environ. 114, 168–182.
Gentine, P., Alemohammad, S.H., 2018. Reconstructed Solar-Induced Fluorescence: A Machine Learning Vegetation Product Based on MODIS Surface Reflectance to Reproduce GOME-2 Solar-Induced Fluorescence. Geophys. Res. Lett. 45, 3136–3146.
Goel, N.S., 1988. Models of vegetation canopy reflectance and their use in estimation of biophysical parameters from reflectance data. Remote Sens. Rev. 4, 1–212.
Guan, K.Y., Berry, J.A., Zhang, Y.G., Joiner, J., Guanter, L., Badgley, G., Lobell, D.B., 2016. Improving the monitoring of crop productivity using spaceborne solar-induced fluorescence. Glob. Change Biol. 22, 716–726.
Guanter, L., Aben, I., Tol, P., Krijger, J.M., Hollstein, A., Köhler, P., Damm, A., Joiner, J., Frankenberg, C., Landgraf, J., 2015. Potential of the TROPOspheric Monitoring Instrument (TROPOMI) onboard the Sentinel-5 Precursor for the monitoring of terrestrial chlorophyll fluorescence. Atmos. Meas. Tech. 8, 1337–1352.
Guanter, L., Zhang, Y., Jung, M., Joiner, J., Voigt, M., Berry, J.A., Frankenberg, C., Huete, A.R., Zarco-Tejada, P., Lee, J.-E., 2014. Global and time-resolved monitoring of crop photosynthesis with chlorophyll fluorescence. Proc. Natl. Acad. Sci. U. S. A 201320008.
He, L.M., Chen, J.M., Liu, J., Mo, G., Joiner, J., 2017. Angular normalization of GOME-2 Sun-induced chlorophyll fluorescence observation as a better proxy of vegetation productivity. Geophys. Res. Lett. 44, 5691–5699.
Houborg, R., Cescatti, A., Migliavacca, M., Kustas, W.P., 2013. Satellite retrievals of leaf chlorophyll and photosynthetic capacity for improved modeling of GPP. Agric. For. Meteorol. 177, 10–23.
Jeong, S.J., Schimel, D., Frankenberg, C., Drewry, D.T., Fisher, J.B., Verma, M., Berry, J.A., Lee, J.E., Joiner, J., 2017. Application of satellite solar-induced chlorophyll fluorescence to understanding large-scale variations in vegetation phenology and function over northern high latitude forests. Remote Sens. Environ. 190, 178–187.
Joiner, J., Guanter, L., Lindstrot, R., Voigt, M., Vasilkov, A.P., Middleton, E.M., Huemmrich, K.F., Yoshida, Y., Frankenberg, C., 2013. Global monitoring of terrestrial chlorophyll fluorescence from moderate-spectral-resolution near-infrared satellite measurements: methodology, simulations, and application to GOME-2. Atmos. Meas. Tech. 6, 2803–2823.
Joiner, J., Yoshida, Y., Guanter, L., Middleton, E.M., 2016. New methods for the retrieval of chlorophyll red fluorescence from hyperspectral satellite instruments: simulations and application to GOME-2 and SCIAMACHY. Atmos. Meas. Tech. 9, 3939–3967.
Joiner, J., Yoshida, Y., Köehler, P., Campbell, P., Frankenberg, C., van der Tol, C., Yang, P., Parazoo, N., Guanter, L., Sun, Y., 2020. Systematic Orbital Geometry-Dependent Variations in Satellite Solar-Induced Fluorescence (SIF) Retrievals. Remote Sens. 12, 2346.
Joiner, J., Yoshida, Y., Vasilkov, A., Schaefer, K., Jung, M., Guanter, L., Zhang, Y., Garrity, S., Middleton, E.M., Huemmrich, K.F., Gu, L., Marchesini, L.B., 2014. The seasonal cycle of satellite chlorophyll fluorescence observations and its relationship to vegetation phenology and ecosystem atmosphere carbon exchange. Remote Sens. Environ. 152, 375–391.

Joiner, J., Yoshida, Y., Vasilkov, A.P., Yoshida, Y., Corp, L.A., Middleton, E.M., 2011. First observations of global and seasonal terrestrial chlorophyll fluorescence from space. Biogeosciences 8, 637–651.
Ju, W.M., Chen, J.M., Black, T.A., Barr, A.G., Liu, J., Chen, B.Z., 2006. Modelling multi-year coupled carbon and water fluxes in a boreal aspen forest. Agric. For. Meteorol. 140, 136–151.
Killi, D., Bussotti, F., Raschi, A., Haworth, M.S., 2017. Adaptation to high temperature mitigates the impact of water deficit during combined heat and drought stress in C3 sunflower and C4 maize varieties with contrasting drought tolerance. Physiol. Plant. 159, 130–147.
Koffi, E.N., Rayner, P.J., Norton, A.J., Frankenberg, C., Scholze, M., 2015. Investigating the usefulness of satellite-derived fluorescence data in inferring gross primary productivity within the carbon cycle data assimilation system. Biogeosciences 12, 4067–4084.
Köhler, P., Frankenberg, C., Magney, T.S., Guanter, L., Joiner, J., Landgraf, J., 2018. Global Retrievals of Solar-Induced Chlorophyll Fluorescence With TROPOMI: First Results and Intersensor Comparison to OCO-2. Geophys. Res. Lett. 45 (10), 456–463.
Kosugi, Y., Matsuo, N., 2006. Seasonal fluctuations and temperature dependence of leaf gas exchange parameters of co-occurring evergreen and deciduous trees in a temperate broad-leaved forest. Tree Physiol 26, 1173–1184.
Lasslop, G., Reichstein, M., Papale, D., Richardson, A.D., Arneth, A., Barr, A., Stoy, P., Wohlfahrt, G., 2010. Separation of net ecosystem exchange into assimilation and respiration using a light response curve approach: critical issues and global evaluation. Glob. Change Biol 16, 187–208.
Lee, J.E., Berry, J.A., Van der Tol, C.S., Yang, X., Guanter, L., Damm, A., Baker, I., Frankenberg, C., 2015. Simulations of chlorophyll fluorescence incorporated into the Community Land Model version 4. Glob. Change Biol. 21, 3469–3477.
Lee, J.E., Frankenberg, C., van der Tol, C., Berry, J.A., Guanter, L., Boyce, C.K., Fisher, J.B., Morrow, E., Worden, J.R., Asefi, S., Badgley, G., 2013. Forest productivity and water stress in Amazonia: Observations from GOSAT chlorophyll fluorescence. Proc. R. Soc. B-Biol. Sci. 280, 20130171.
Leuning, R., Cleugh, H.A., Zegelin, S.J., Hughes, D., 2005. Carbon and water fluxes over a temperate Eucalyptus forest and a tropical wet/dry savanna in Australia: measurements and comparison with MODIS remote sensing estimates. Agric. For. Meteorol. 129, 151–173.
Li, X., Xiao, J., He, B., 2018a. Chlorophyll fluorescence observed by OCO-2 is strongly related to gross primary productivity estimated from flux towers in temperate forests. Remote Sens. Environ. 204, 659–671.
Li, X., Xiao, J.F., 2019. A Global, 0.05-Degree Product of Solar-Induced Chlorophyll Fluorescence Derived from OCO-2, MODIS, and Reanalysis Data. Remote Sens 11, 517.
Li, X., Xiao, J.F., He, B.B., Arain, M.A., Beringer, J., Desai, A.R., Emmel, C., Hollinger, D.Y., Krasnova, A., Mammarella, I., Noe, S.M., Ortiz, P.S., Rey-Sanchez, A.C., Rocha, A.V., Varlagin, A., 2018b. Solar-induced chlorophyll fluorescence is strongly correlated with terrestrial photosynthesis for a wide variety of biomes: First global analysis based on OCO-2 and flux tower observations. Glob. Change Biol. 24, 3990–4008.
Liu, J., Chen, J., Cihlar, J., Park, W., 1997. A process-based boreal ecosystem productivity simulator using remote sensing inputs. Remote Sens. Environ. 62, 158–175.
Liu, L., Liu, X., Guan, L., 2016a. Uncertainties in linking solar-induced chlorophyll fluorescence to plant photosynthetic activities. In: Proceedings of the IEEE InternationalGeoscience and Remote Sensing Symposium (IGARSS). IEEE, pp. 4414–4417.
Liu, L.Y., Cheng, Z.H., 2010. Detection of vegetation light-use efficiency based on solar-induced chlorophyll fluorescence separated from canopy radiance spectrum. IEEE J. Sel. Top. Appl. Earth Observ. Remote Sens. 3, 306–312.
Liu, L.Y., Guan, L.L., Liu, X.J., 2017a. Directly estimating diurnal changes in GPP for C3 and C4 crops using far-red sun-induced chlorophyll fluorescence. Agric. For. Meteorol. 232, 1–9.
Liu, L.Y., Liu, X.J., Hu, J.C., Guan, L.L., 2017b. Assessing the wavelength-dependent ability of solar-induced chlorophyll fluorescence to estimate the GPP of winter wheat at the canopy level. Int. J. Remote Sens. 38, 4396–4417.
Liu, L.Y., Liu, X.J., Wang, Z.H., Zhang, B., 2016b. Measurement and Analysis of Bidirectional SIF Emissions in Wheat Canopies. IEEE Trans. Geosci. Remote Sensing 54, 2640–2651.
Liu, W.W., Atherton, J., Mottus, M., Gastellu-Etchegorry, J.P., Malenovsky, Z., Raumonen, P., Akerblom, M., Makipaa, R., Porcar-Castell, A., 2019. Simulating solar-induced chlorophyll fluorescence in a boreal forest stand reconstructed from terrestrial laser scanning measurements. Remote Sens. Environ. 232.
Liu, X., Guanter, L., Liu, L., Damm, A., Malenovský, Z., Rascher, U., Peng, D., Du, S., Gastellu-Etchegorry, J.-P., 2018a. Downscaling of solar-induced chlorophyll fluorescence from canopy level to photosystem level using a random forest model. Remote Sens. Environ.
Liu, X., Liu, L., Hu, J., Guo, J., Du, S., 2020. Improving the potential of red SIF for estimating GPP by downscaling from the canopy level to the photosystem level. Agricult. Forest Meteorol. 281, 107846.
Liu, Y., Wang, J., Yao, L., Chen, X., Cai, Z., Yang, D., Yin, Z., Gu, S., Tian, L., Lu, N., 2018b. The TanSat mission: preliminary global observations. Sci. Bull. 63, 1200–1207.
Matsushita, B., Tamura, M., 2002. Integrating remotely sensed data with an ecosystem model to estimate net primary productivity in East Asia. Remote Sens. Environ. 81, 58–66.
Mo, X.G., Chen, J.M., Ju, W.M., Black, T.A., 2008. Optimization of ecosystem model parameters through assimilating eddy covariance flux data with an ensemble Kalman filter. Ecol. Model. 217, 157–173.
Mohammed, G.H., Colombo, R., Middleton, E.M., Rascher, U., van der Tol, C., Nedbal, L., Goulas, Y., Pérez-Priego, O., Damm, A., Meroni, M., 2019. Remote sensing of solar-induced chlorophyll fluorescence (SIF) in vegetation: 50 years of progress. Remote Sens. Environ. 231, 111177.
Myneni, R., Knyazikhin, Y., Park, T.2015. MCD15A2H MODIS/Terra+ Aqua Leaf Area Index/FPAR 8-day L4 Global 500m SIN Grid V006. NASA EOSDIS Land Processes DAAC.
Nachtergaele, F., van Velthuizen, H., Verelst, L., Batjes, N., Dijkshoorn, K., van Engelen, V., Fischer, G., Jones, A., Montanarela, L., 2010. The harmonized world soil database. In: Proceedings of the 19th World Congress of Soil Science, Soil Solutions for a Changing World. Brisbane, Australia. pp. 34–37 1-6 August 2010.
Norman, J.M., 1982. Simulation of microclimates. Biometeorol. Integrated Pest Manag. 65–99.
Norton, A.J., Rayner, P.J., Koffi, E.N., Scholze, M., Silver, J.D., Wang, Y.P., 2019. Estimating global gross primary productivity using chlorophyll fluorescence and a data assimilation system with the BETHY-SCOPE model. Biogeosciences 16, 3069–3093.
Pacheco-Labrador, J., El-Madany, T.S., van der Tol, C., Martín, M.P., Gonzalez-Cascon, R., Perez-Priego, O., Guan, J., Moreno, G., Carrara, A., Reichstein, M., Migliavacca, M. 2020. senSCOPE: Modeling radiative transfer and biochemical processes in mixed canopies combining green and senescent leaves with SCOPE. bioRxiv, 2020.02.05. 935064.
Parazoo, N.C., Magney, T., Norton, A., Raczka, B., Bacour, C., Maignan, F., Baker, I., Zhang, Y., Qiu, B., Shi, M., MacBean, N., Bowling, D.R., Burns, S.P., Blanken, P.D., Stutz, J., Grossman, K., Frankenberg, C., 2020. Wide Discrepancies in the Magnitude and Direction of Modelled SIF in Response to Light Conditions. Biogeosci. Discuss. 2020, 1–42.
Pastorello, G., Papale, D., Chu, H., Trotta, C., Agarwal, D., Canfora, E., Baldocchi, D., Torn, M., 2017. A new data set to keep a sharper eye on land-air exchanges. Eos 98. https://doi.org/10.1029/2017EO071597.
Porcar-Castell, A., Tyystjarvi, E., Atherton, J., van der Tol, C., Flexas, J., Pfundel, E.E., Moreno, J., Frankenberg, C., Berry, J.A., 2014. Linking chlorophyll a fluorescence to photosynthesis for remote sensing applications: mechanisms and challenges. J. Exp. Bot. 68, 2453 -2453.
Qiu, B., Chen, J.M., Ju, W., Zhang, Q., Zhang, Y., 2019. Simulating emission and scattering of solar-induced chlorophyll fluorescence at far-red band in global vegetation with different canopy structures. Remote Sens. Environ. 233, 111373.
Qiu, B., Xue, Y., Fisher, J.B., Guo, W., Berry, J.A., Zhang, Y., 2018. Satellite Chlorophyll Fluorescence and Soil Moisture Observations Lead to Advances in the Predictive Understanding of Global Terrestrial Coupled Carbon-Water Cycles. Glob. Biogeochem. Cycle 32, 360–375.
Raczka, B., Porcar-Castell, A., Magney, T., Lee, J., Köhler, P., Frankenberg, C., Grossmann, K., Logan, B., Stutz, J., Blanken, P., 2019. Sustained nonphotochemical quenching shapes the seasonal pattern of solar-induced fluorescence at a high-elevation evergreen forest. J. Geophys. Res. Biogeosci. 124, 2005–2020.
Reichstein, M., Tenhunen, J., Roupsard, O., Ourcival, J.M., Rambal, S., Miglietta, F., Peressotti, A., Pecchiari, M., Tirone, G., Valentini, R., 2003. Inverse modeling of seasonal drought effects on canopy CO_2/H_2O exchange in three Mediterranean ecosystems. J. Geophys. Res. Atmosph. 108.
Reick, C., Raddatz, T., Brovkin, V., Gayler, V., 2013. Representation of natural and anthropogenic land cover change in MPI-ESM. J. Adv. Model. Earth Syst. 5, 459–482.
Revill, A., Sus, O., Barrett, B., Williams, M., 2013. Carbon cycling of European croplands: A framework for the assimilation of optical and microwave Earth observation data. Remote Sens. Environ. 137, 84–93.
Rochdi, N., Fernandes, R., Chelle, M., 2006. An assessment of needles clumping within shoots when modeling radiative transfer within homogeneous canopies. Remote Sens. Environ. 102, 116–134.
Rodell, M., Houser, P.R., Jambor, U., Gottschalck, J., Mitchell, K., Meng, C.J., Arsenault, K., Cosgrove, B., Radakovich, J., Bosilovich, M., Entin, J.K., Walker, J.P., Lohmann, D., Toll, D., 2004. The global land data assimilation system. Bull. Amer. Meteorol. Soc. 85, 381–394.
Scholes, R., Gureja, N., Giannecchinni, M., Dovie, D., Wilson, B., Davidson, N., Piggott, K., McLoughlin, C., Van der Velde, K., Freeman, A.J.K., 2001. The environment and vegetation of the flux measurement site near Skukuza. Kruger National Park. Koedoe 44, 73–83.
Shan, N., Ju, W.M., Migliavacca, M., Martin, D., Guanter, L., Chen, J.M., Goulas, Y., Zhang, Y.G., 2019. Modeling canopy conductance and transpiration from solar-induced chlorophyll fluorescence. Agric. For. Meteorol. 268, 189–201.
Sims, D.A., Rahman, A.F., Cordova, V.D., Baldocchi, D.D., Flanagan, L.B., Goldstein, A.H., Hollinger, D.Y., Misson, L., Monson, R.K., Schmid, H.P., Wofsy, S.C., Xu, L.K., 2005. Midday values of gross CO_2 flux and light use efficiency during satellite overpasses can be used to directly estimate eight-day mean flux. Agric. For. Meteorol. 131, 1–12.
Sulla-Menashe, D., Friedl, M.A.2018. User Guide to Collection 6 MODIS Land Cover (MCD12Q1 and MCD12C1) Product.
Sun, Y., Frankenberg, C., Jung, M., Joiner, J., Guanter, L., Köhler, P., Magney, T., 2018. Overview of Solar-Induced chlorophyll Fluorescence (SIF) from the Orbiting Carbon Observatory-2: Retrieval, cross-mission comparison, and global monitoring for GPP. Remote Sens. Environ. 209, 808–823.
Sun, Y., Frankenberg, C., Wood, J.D., Schimel, D.S., Jung, M., Guanter, L., Drewry, D., Verma, M., Porcar-Castell, A., Griffis, T.J., 2017. OCO-2 advances photosynthesis observation from space via solar-induced chlorophyll fluorescence. Science 358 eaam5747.
Suyker, A.E., Verma, S.B., Burba, G.G., Arkebauer, T.J., 2005. Gross primary production and ecosystem respiration of irrigated maize and irrigated soybean during a growing season. Agricult. Forest Meteorol. 131, 180–190.
Thum, T., Zaehle, S., Köhler, P., Aalto, T., Aurela, M., Guanter, L., Kolari, P., Laurila, T., Lohila, A., Magnani, F., Van der Tol, C., Markkanen, T., 2017. Modelling sun-induced fluorescence and photosynthesis with a land surface model at local and regional

scales in northern Europe. Biogeosciences 14, 1969–1987.
Thurner, M., Beer, C., Santoro, M., Carvalhais, N., Wutzler, T., Schepaschenko, D., Shvidenko, A., Kompter, E., Ahrens, B., Levick, S.R., Schmullius, C., 2014. Carbon stock and density of northern boreal and temperate forests. Glob. Ecol. Biogeogr. 23, 297–310.
Turner, A.J., Köhler, P., Magney, T.S., Frankenberg, C., Fung, I., Cohen, R.C., 2020. A double peak in the seasonality of California's photosynthesis as observed from space. Biogeosciences 17, 405–422.
van der Tol, C., Berry, J.A., Campbell, P.K.E., Rascher, U., 2014. Models of fluorescence and photosynthesis for interpreting measurements of solar-induced chlorophyll fluorescence. J. Geophys. Res. Biogeosci. 119, 2312–2327.
van der Tol, C., Verhoef, W., Timmermans, J., Verhoef, A., Su, Z., 2009. An integrated model of soil-canopy spectral radiances, photosynthesis, fluorescence, temperature and energy balance. Biogeosciences 6, 3109–3129.
van der Tol, C., Vilfan, N., Dauwe, D., Cendrero-Mateo, M.P., Yang, P., 2019. The scattering and re-absorption of red and near-infrared chlorophyll fluorescence in the models Fluspect and SCOPE. Remote Sens. Environ. 232, 111292.
Van Wittenberghe, S., Alonso, L., Verrelst, J., Moreno, J., Samson, R., 2015. Bidirectional sun-induced chlorophyll fluorescence emission is influenced by leaf structure and light scattering properties - A bottom-up approach. Remote Sens. Environ. 158, 169–179.
Verhoef, W., 2011. Modelling vegetation fluorescence observations. In: Proceedings of the 7th EARSEL workshop of the Special Interest Group in Imaging Spectroscopy: Final Programme. Edinburgh, UK. 11-13 April 2011.
Verhoef, W., Bach, H., 2007. Coupled soil–leaf-canopy and atmosphere radiative transfer modeling to simulate hyperspectral multi-angular surface reflectance and TOA radiance data. Remote Sens. Environ. 109, 166–182.
Verhoef, W., Jia, L., Xiao, Q., Su, Z., 2007. Unified optical-thermal four-stream radiative transfer theory for homogeneous vegetation canopies. IEEE Trans. Geosci. Remote Sensing 45, 1808–1822.
Verrelst, J., Rivera, J.P., van der Tol, C., Magnani, F., Mohammed, G., Moreno, J., 2015. Global sensitivity analysis of the SCOPE model: What drives simulated canopy-leaving sun-induced fluorescence? Remote Sens. Environ. 166, 8–21.
Verrelst, J., van der Tol, C., Magnani, F., Sabater, N., Rivera, J.P., Mohammed, G., Moreno, J., 2016. Evaluating the predictive power of sun-induced chlorophyll fluorescence to estimate net photosynthesis of vegetation canopies: A SCOPE modeling study. Remote Sens. Environ. 176, 139–151.
Vilfan, N., van der Tol, C., Muller, O., Rascher, U., Verhoef, W., 2016. Fluspect-B: A model for leaf fluorescence, reflectance and transmittance spectra. Remote Sens. Environ. 186, 596–615.
Wang, Y., Jarvis, P., 1990. Influence of crown structural properties on PAR absorption, photosynthesis, and transpiration in Sitka spruce: application of a model (MAESTRO). Tree Physiol 7, 297–316.
Wang, Y.-P., Leuning, R., 1998. A two-leaf model for canopy conductance, photosynthesis and partitioning of available energy I: Model description and comparison with a multi-layered model. Agricult. Forest Meteorol. 91, 89–111.
Wang, Z., 2014. Sunlit Leaf Photosynthesis Rate Correlates Best with Chlorophyll Fluorescence of Terrestrial Ecosystems. M.D. Thesis. University of Toronto.
Xiao, Z.Q., Liang, S.L., Wang, J.D., Chen, P., Yin, X.J., Zhang, L.Q., Song, J.L., 2014. Use of General Regression Neural Networks for Generating the GLASS Leaf Area Index Product From Time-Series MODIS Surface Reflectance. IEEE Trans. Geosci. Remote Sensing 52, 209–223.
Xiao, Z.Q., Liang, S.L., Wang, J.D., Xiang, Y., Zhao, X., Song, J.L., 2016. Long-Time-Series Global Land Surface Satellite Leaf Area Index Product Derived From MODIS and AVHRR Surface Reflectance. IEEE Trans. Geosci. Remote Sensing 54, 5301–5318.
Yang, P.Q., van der Tol, C., 2018. Linking canopy scattering of far-red sun-induced chlorophyll fluorescence with reflectance. Remote Sens. Environ. 209, 456–467.
Yang, X., Tang, J., Mustard, J.F., Lee, J.E., Rossini, M., Joiner, J., Munger, J.W., Kornfeld, A., Richardson, A.D., 2015. Solar-induced chlorophyll fluorescence that correlates with canopy photosynthesis on diurnal and seasonal scales in a temperate deciduous forest. Geophys. Res. Lett. 42, 2977–2987.
Zarco-Tejada, P.J., Catalina, A., Gonzalez, M.R., Martin, P., 2013. Relationships between net photosynthesis and steady-state chlorophyll fluorescence retrieved from airborne hyperspectral imagery. Remote Sens. Environ. 136, 247–258.
Zeng, Y., Badgley, G., Dechant, B., Ryu, Y., Chen, M., Berry, J.A., 2019. A practical approach for estimating the escape ratio of near-infrared solar-induced chlorophyll fluorescence. Remote Sens. Environ. 232, 111209.
Zhang, F.M., Chen, J.M., Chen, J.Q., Gough, C.M., Martin, T.A., Dragoni, D., 2012. Evaluating spatial and temporal patterns of MODIS GPP over the conterminous US against flux measurements and a process model. Remote Sens. Environ. 124, 717–729.
Zhang, Y., 2011. Forest leaf chlorophyll study using hyperspectral remote sensing. Hyperspectral Remote Sensing Vegetat. 167–186.
Zhang, Y., Joiner, J., Alemohammad, S.H., Zhou, S., Gentine, P., 2018a. A global spatially contiguous solar-induced fluorescence (CSIF) dataset using neural networks. Biogeosciences 15, 5779–5800.
Zhang, Y., Xiao, X.M., Jin, C., Dong, J.W., Zhou, S., Wagle, P., Joiner, J., Guanter, L., Zhang, Y.G., Zhang, G.L., Qin, Y.W., Wang, J., Moore, B., 2016a. Consistency between sun-induced chlorophyll fluorescence and gross primary production of vegetation in North America. Remote Sens. Environ. 183, 154–169.
Zhang, Y.G., Guanter, L., Berry, J.A., Joiner, J., van der Tol, C., Huete, A., Gitelson, A., Voigt, M., Köhler, P., 2014. Estimation of vegetation photosynthetic capacity from space-based measurements of chlorophyll fluorescence for terrestrial biosphere models. Glob. Change Biol. 20, 3727–3742.
Zhang, Y.G., Guanter, L., Berry, J.A., van der Tol, C., Yang, X., Tang, J.W., Zhang, F.M., 2016b. Model-based analysis of the relationship between sun-induced chlorophyll fluorescence and gross primary production for remote sensing applications. Remote Sens. Environ. 187, 145–155.
Zhang, Y.G., Guanter, L., Joiner, J., Song, L., Guan, K.Y., 2018c. Spatially-explicit monitoring of crop photosynthetic capacity through the use of space-based chlorophyll fluorescence data. Remote Sens. Environ. 210, 362–374.
Zhang, Y.Q., Chen, J.M., Miller, J.R., Noland, T.L., 2008. Retrieving chlorophyll content in conifer needles from hyperspectral measurements. Can. J. Remote Sens. 34, 296–310.
Zhao, F., Dai, X., Verhoef, W., Guo, Y.Q., van der Tol, C., Li, Y.G., Huang, Y.B., 2016. FluorWPS: A Monte Carlo ray-tracing model to compute sun-induced chlorophyll fluorescence of three-dimensional canopy. Remote Sens. Environ. 187, 385–399.